國 立 交 通 大 學
光 電 工 程 研 究 所

碩 士 論 文

使用量子點雷射減慢光訊息行進速度

Slowing Light Using Quantum-Dot Laser Amplifiers

研 究 生：劉瑞農
指導教授：郭浩中 教授
盧廷昌 教授

中 華 民 國 九 十 六 年 八 月

使用量子點雷射減慢光訊息行進速度

Slowing Light Using Quantum-Dot Laser Amplifiers

研 究 生：劉瑞農　　Student：Jui-Nung Liu

指導教授：郭浩中　　Advisor：Hao-Chung Kuo

盧廷昌　　Tien-Chang Lu

國 立 交 通 大 學

光 電 工 程 研 究 所

碩 士 論 文

A Thesis

Submitted to Institute of Electro-Optical Engineering

College of Electrical Engineering and Computer Science

National Chiao Tung University

in partial Fulfillment of the Requirements

for the Degree of Master

in

Electro-Optical Engineering

August 2007

Hsinchu, Taiwan, Republic of China

中 華 民 國 九 十 六 年 八 月

使用量子點雷射減慢光訊息行進速度

研究生：劉瑞農　　指導教授：郭浩中 教授、盧廷昌 教授

國立交通大學 光電工程研究所

摘 要

本論文旨在探索半導體雷射於作為慢光元件之新穎用途。針對之前實驗所觀察量子點面射型雷射的慢光現象進行探討，並使用雷射放大器模型進行理論模擬。模擬結果解釋了光訊息速度隨著雷射增益加大而減慢，以及隨者調變頻率增高而加快等實驗上觀察到的現象。此外，針對實驗尚未研究的部份，模擬結果預測了 1 至 5 GHz 的光訊息在該雷射元件之行進速度。在另一方面，本論文從實驗的角度探索了使用半導體雷射外部注入光之技術來減慢光資訊速度之可能。利用網路分析儀所量測到的相位響應顯示有可能達成接近 360 度的 RF 訊號延遲。光譜資料顯示了這樣的 RF 延遲與光訊息被不對稱的放大有關。

Slowing Light Using Quantum-Dot Laser Amplifiers

Student：Jui-Nung Liu **Advisors：Dr. Hao-Chung Kuo**
Dr. Tien-Chang Lu

Institute of Electro-Optical Engineering
National Chiao Tung University

ABSTRACT

This thesis explores the novel use of semiconductor lasers as optical delay lines. Slowing light using vertical-cavity surface-emitting lasers (VCSELs) is explained and simulated using the VCSEL amplifier model. Simulated results and experimental result are qualitatively in a good agreement. With the aid of the filter phase analysis, the simulations explain that group delay increases with increased modal gain and decreases with increased modulation frequency. Besides, the simulations predict the VCSEL's capability of delaying single-tone sinusoidal signal of 1 to 5 GHz. On the other hand, RF delay or optical delay using injection-locking of VCSELs is studied experimentally in the thesis. Optical spectra show that the VCSEL is not in the stable-locking range. The VCSEL acts as a regenerative amplifier, making one of the signal side band much larger than the other.

ACKNOWLEDGEMENT

時光飛逝，轉眼間要畢業了。碩士論文能夠順利完成，首先要感謝郭浩中老師的賞識，賦予我這個挑戰性高、需要量子電子學理論與通訊實驗技術兩者兼備的研究題目。另外，王興宗老師對於學問研究的熱忱與毅力，深深地影響我做學問的態度。感謝彭朋群博士在光通訊實驗的指導與全力協助。感謝盧老師的指導。感謝林俊廷博士與文凱在實驗上的幫忙。感謝工研院奈米光電中心祁錦雲博士、林國瑞博士與楊泓彬博士在量子點雷射元件的提供，使我得以一窺奈米技術在光電領域的運用。此外，感謝李建平老師對我在量子與固態物理學的啟蒙，使我堅信憑著這股興趣可以讓自己在人生的路上走得更遠，並對社會產生更大的貢獻。感謝莊順連教授的鼓勵，使我有了靈感與不眠不休的衝勁，因而得以完成這份論文的主要模擬部份。

感謝實驗室師兄姐：鴻儒、小朱、小強、芳儀、宗鼎、剛帆、志堯、柏傑、清華、明華、俊榮、士偉、貽安、宗憲與姚忻宏的幫忙與指點。感謝同學：碩均、金門、孟儒、潤琪、家璞、卓奕與秉寬的扶持。感謝401實驗室的學弟妹：晁恩、柏源、伯駿、家銘、昀恬、尚樺的陪伴，祝你們將來都順順利利的。

最後，要感謝我的家人，你們在背後的支持提供了我克服困難的動力。

劉瑞農

新竹交通大學

2007年秋

TABLE OF CONTENTS

LIST OF FIGURES

CHAPTER 2

CHAPTER 3

CHAPTER 4

Chapter 1

INTRODUCTION

Semiconductor optoelectronics deals with the interaction between electrons and photons in the semiconductor materials and devices [1, 2]. Form an applied physicist's point of view, semiconductor optoelectronics is an exciting application of quantum mechanics. In order to describe how electrons interact with photons, semi classical treatment which treats photons as a perturbation field [3], or all quantum-mechanically approach which sees photons as quanta [2], is needed. Besides, to design semiconductor materials and devices, quantum mechanics is necessary to understand the crystal band structure, quantized electronic quantum states in a low-dimensional nanostructure, and the working principle of the devices.

We have witnessed the great impact of the semiconductor optoelectronics on both our everyday lives and scientific interests. One successful example is the quantum-well semiconductor laser. Thanks modern heteroepitaxy techniques such as molecular beam epitaxy (MBE) and metal-organic chemical vapor deposition (MOCVD), high-quality quantum-well lasers can be made. Today, the quantum-well semiconductor laser is found in virtually every home as part of the compact-disc (CD)

player [4].

On the other hand, the success in the growth of quantum-well structure makes a study of the introductory quantum physics realizable in these artificial semiconductor structures [3]. Semiconductor heterostructures and especially low-dimensional nanostructures such as quantum wells (QW), quantum wires, and quantum dots (QD), currently comprise the object of investigation of two thirds of all research groups in the physics of semiconductors [4]. Among them, a QD mimics the basic properties of an atom providing a geometrical size allowing the practical application of atomic physics to the field of semiconductor devices [5]. In the optoelectronics applications, quantum-dot lasers are expected to show a broader modulation bandwidth, higher temperature stability and lower power consumption than quantum-well counterparts, primarily due to the discrete energy states of electrons and holes under three-dimensional quantum confinement by quantum dots [6]. At the beginning of the 1990s it was realized that universal self-organization on surfaces in lattice mismatched heteroepitaxial growth can be used to form high densities of homogenous QDs [7]. Recently, owing to the developments of high-density and high-quality InAs-based self-assembled quantum dots, semiconductor lasers using semiconductor quantum dots in the wavelength range of 1.3–1.6μm have improved in their performances remarkably [6]. Therefore, QD lasers are very promising for new generations of edge-emitting lasers (EEL) and vertical-cavity surface-emitting lasers (VCSEL) in communication.

In addition to the development of the semiconductor lasers with low-dimensional gain materials, one of the remaining grand challenges in optoelectronic technology is the ability to store an optical signal in optical format [8]. Slow light, i.e. optical signal propagating at a velocity much slower than the speed of light in the vacuum, has attracted unprecedented attentions in the past few years [9]. Various mechanisms have been used to obtain a large material dispersion for achieving slow light on semiconductor platform [8, 9]. Among these methods, slowing light using quantum-well Fabry-Perot laser [10], quantum-well VCSEL [11], and quantum-dot VCSEL [12] creates new application of semiconductor lasers in communication in addition to serving as optical transmitters. Especially, large delay-bandwidth product (DBP) using surface-emitting lasers are experimentally demonstrated [11, 12], but few theoretical explanation and analysis are given.

The outline of this thesis is as follows.

- Chapter 2 gives an introduction to semiconductor optoelectronics and semiconductor lasers
- Chapter 3 first reviews the previous experimental work in [12] and subsequently utilizes VCSEL amplifier model to explain this novel slow-light phenomenon with VCSEL.
- Chapter 4 studies RF delay or optical delay using injection-locking technique of semiconductor lasers.
- The last chapter concludes the research study, and presents some future

work.

Chapter 2

SEMICONDUCTOR LASERS AND LOW-DIMENSIONAL GAIN MATERIALS

2.1 INTRODUCTION

In this chapter, the basic theory of the semiconductor band structure using Kane's $k \cdot p$ model and low-dimensional nanostructures will be reviewed first. Subsequently, electron-photon interaction in semiconductors and its low-dimensional structures will be described using semi-classical approach. Then we will review one of the most important device applications of semiconductor optoelectronics – semiconductor lasers, and vertical-cavity surface-emitting lasers (VCSELs) will then be addressed. Afterward, semiconductor lasers with low-dimensional gain materials will be discussed.

2.2 KANE'S $k \cdot p$ THEORY FOR SEMICONDUCTOR BAND STRUCTURE [3, 13, 14]

A semiconductor crystal has a periodic arrangement of the atoms, and then has a periodic electronic potential $V(\vec{r}) = V(\vec{r} + \bar{\mathrm{T}})$, where $\bar{\mathrm{T}}$ is the translational vector of

the crystal lattice. Fig. 2.1 shows schematic plot of the periodic potential in a one-dimensional crystal.

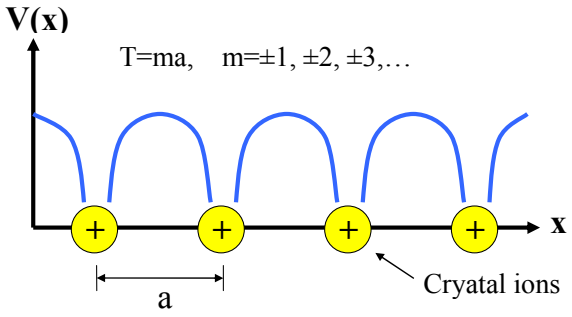

Figure 2.1. Schematic periodic potential in a one-dimensional crystal.

To describe the behavior of an electron in the semiconductor crystal, we must solve the eigenstates of the time-independent Schrödinger equation:

$$\hat{H}\psi(\vec{r})_{n,\vec{k}} = [-\frac{\hbar^2}{2m_0}\nabla^2 + V(\vec{r})]\psi_{n,\vec{k}} = E_{n,\vec{k}} \cdot \psi_{n,\vec{k}}(\vec{r}) . \quad (1.1)$$

Besides, for an electron in a periodic potential, Bloch theorem requires that

$$\psi_{n,\vec{k}}(\vec{r}) = u_{n,\vec{k}}(\vec{r}) \cdot e^{i\vec{k}\cdot\vec{r}} . \quad (1.2)$$

Therefore, the Schrödinger equation can be rewritten as

$$[-\frac{\hbar^2}{2m_0}\nabla^2 + V(\vec{r}) + \frac{\hbar}{m_0}\vec{k}\cdot\vec{p}]u_{n,\vec{k}} = (E_{n,\vec{k}} - \frac{\hbar^2 k^2}{2m_0}) \cdot u_{n,\vec{k}}(\vec{r}) \quad (1.3)$$

At the zone center (k=0), we can solve the energy eigenstates. Because the Hamiltonian operator is hermitian, the eigenstates not in the zone center can be presented as the linear combination of the eigenstates at the zone center. Using the eigenstates at the zone center as the basis, we can get

$$u_{n,\vec{k}}(\vec{r}) = \sum_m C^m_{n,k} \cdot u_{n,\vec{k}=0}(\vec{r}) \tag{1.4}$$

Use (1.4) in (1.3), we have

$$[E_{M,k=0} + \frac{\hbar^2}{2m_0}k^2 - E_{n,\vec{k}}]C^m_{n,k} + \sum_m H^{kp}_{Mn} \cdot C^m_{n,k} = 0 \tag{1.5}$$

where

$$H^{kp}_{Mm} = \frac{\hbar}{m_o}\vec{k} \cdot \langle u_{M,k=0} | \hat{p} | u_{m,k=0} \rangle . \tag{1.6}$$

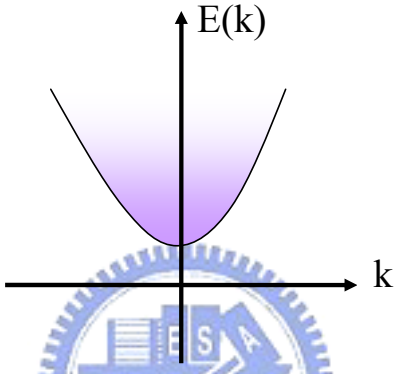

Figure 2.2. A single-band in the $k \cdot p$ method.

For a single band, such as the band edge of conduction band (Fig. 2.2), using (1.3) and the time-independent perturbation theory to the second order, we can get

$$\mathrm{E}_{n,k} - \frac{\hbar^2 k^2}{2m_0} = E_{n,k=0} + \frac{\hbar}{m_0}\vec{k} \cdot \langle u_{n,k=0} | \hat{p} | u_{n,k=0} \rangle + \frac{\hbar^2}{{m_0}^2} \cdot \sum_{n' \neq n} \frac{\left| \vec{k} \cdot \langle u_{n,k=0} | \hat{p} | u_{n',k=0} \rangle \right|^2}{E_{n,\vec{k}=0} - E_{n',\vec{k}=0}} \tag{1.7}$$

Therefore, we can have

$$\mathrm{E}_{n,\vec{k}} - E_{n,\vec{k}=0} = \sum_{\alpha,\beta=x,y,z} D^{\alpha\beta} \cdot k_\alpha \cdot k_\beta \tag{1.8}$$

$$\mathrm{D}^{\alpha\beta} = \frac{\hbar^2}{2}(\frac{1}{m*})_{\alpha,\beta} = \frac{\hbar^2}{2m_0}\delta_{\alpha,\beta} + \frac{\hbar^2}{{2m_0}^2} \sum_{n' \neq n} \frac{P^\alpha_{nn'} \cdot P^\beta_{nn'} + P^\beta_{nn'} P^\alpha_{nn'}}{E_{n,\vec{k}=0} - E_{n',\vec{k}=0}} \tag{1.9}$$

where $P_{nn'}$ is the momentum matrix element. According to (1.8), the eigen-energy near the band edge is in the quadratic form.

2.2.1 Kane's $k \bullet p$ Model with the Spin-Orbit Interaction

If the spin-orbit interaction is taken into account, we add a spin-orbit interaction term in the Hamiltonian. Because spin-orbit interaction perturbation is proportional to $\mathrm{L} \cdot \mathrm{S}$, where L and S are the orbit angular momentum and the spin angular momentum, respectively. Thus, we have the total Hamiltonian

$$\mathrm{H} = -\frac{\hbar^2}{2m_0}\nabla^2 + V(\vec{r}) + \lambda\frac{\hbar^2}{2}(J^2 - L^2 - S^2)\,. \tag{1.10}$$

Use this total Hamiltonian and the Bloch theorem, the Schrödinger equation becomes

$$[-\frac{\hbar^2}{2m_0}\nabla^2 + V(\vec{r}) + \frac{\hbar}{m_0}\vec{k}\cdot\vec{p} + \lambda\frac{\hbar^2}{2}(J^2 - L^2 - S^2)]u_{n,\vec{k}} = (E_{n,\vec{k}} - \frac{\hbar^2 k^2}{2m_0})\cdot u_{n,\vec{k}}(\vec{r})\,. \tag{1.11}$$

At the zone center,

$$[-\frac{\hbar^2}{2m_0}\nabla^2 + V(\vec{r}) + \lambda\frac{\hbar^2}{2}(J^2 - L^2 - S^2)]u_{n,\vec{k}=0} = E_{n,\vec{k}=0}\cdot u_{n,\vec{k}=0}(\vec{r})\,. \tag{1.12}$$

The solutions of the above equation form a complete set, so we can expand the eigenstate not in the zone center as the linear combination of the complete set at zone center. Because the total angular momentum J, the orbit angular momentum L, the spin angular momentum S, and $\mathrm{L} \cdot \mathrm{S}$ coupling term commute with each other, they can have common complete set of eigenfunctions. Since s=1/2 for electron, we can denote the eigenstates of these operators as $\left|j, m_j, l\right\rangle$ in Dirac notation, where the

items in the "ket" are the quantum numbers corresponding their physical operators.

Assume $\hat{\mathrm{H}}_0|S\rangle = E_s|S\rangle$ and $\hat{\mathrm{H}}_0\left|j=1,m_j\right\rangle = E_p\left|j=1,m_j\right\rangle$, and choose the basis functions

$$\begin{aligned}&|iS\uparrow\rangle,|iS\downarrow\rangle,|Z\uparrow\rangle,|Z\downarrow\rangle,\\&\left|\frac{X-iY}{\sqrt{2}}\uparrow\right\rangle,\left|-\frac{X-iY}{\sqrt{2}}\downarrow\right\rangle,\left|-\frac{X+iY}{\sqrt{2}}\uparrow\right\rangle,\left|\frac{X+iY}{\sqrt{2}}\downarrow\right\rangle.\end{aligned} \tag{1.13}$$

Then we can have an 8x8 interaction matrix

$$[\mathrm{H}]=\begin{bmatrix}\overline{\overline{H}} & 0\\ 0 & \overline{\overline{H}}\end{bmatrix} \tag{1.14}$$

where, assuming $\vec{k}=k\hat{z}$ is in the z-direction, the 4x4 matrix $\overline{\overline{\mathrm{H}}}$ is

$$\overline{\overline{\mathrm{H}}}=\begin{bmatrix}E_s & 0 & kP & 0\\ 0 & E_p-\frac{\Delta}{3} & \frac{\sqrt{2}\Delta}{3} & 0\\ kP & \frac{\sqrt{2}\Delta}{3} & E_p & 0\\ 0 & 0 & 0 & E_p+\frac{\Delta}{3}\end{bmatrix} \tag{1.15}$$

where

$$\mathrm{P}=-i\frac{\hbar}{m_0}\langle S|\hat{P}_z|Z\rangle \tag{1.16}$$

is the Kane's parameter, and $\Delta = 3\frac{\lambda\hbar^2}{2}$.

Solving the eigenvalue problem

$$\left|[\mathrm{H}]-\mathrm{E}'\cdot\overline{\overline{\mathrm{I}}}\right|=0 \tag{1.17}$$

, we can obtain the energy eigenvalues *near* the zone center:

$$E_c = E_g + \frac{k^2 P^2 (E_g + \frac{2}{3}\Delta)}{E_g (E_g + \Delta)} = E_g + \frac{\hbar^2 k^2}{2m_c *} \text{ (Conduction band, C)} \quad (1.18)$$

$$E_{hh} = \frac{\hbar^2 k^2}{2m_0} \text{ (Heavy - hole band, HH)} \quad (1.19)$$

$$E_{lh} = -\frac{2k^2 P^2}{3E_g} = -\frac{\hbar^2 k^2}{2m_{lh} *} \text{ (Light - hole band)} \quad (1.20)$$

$$E_{so} = -\frac{k^2 P^2}{3(E_g + \Delta)} = -\Delta - \frac{\hbar^2 k^2}{2m_{so}} \text{ (Split - off band)} \quad (1.21)$$

Note that the conduction band effective mass increase with increased band gap of a semiconductor material. The Kane's model indicates positive effective mass for heavy-hole band, and this is corrected in the Luttinger-Kuhn model [3, 14, 15].

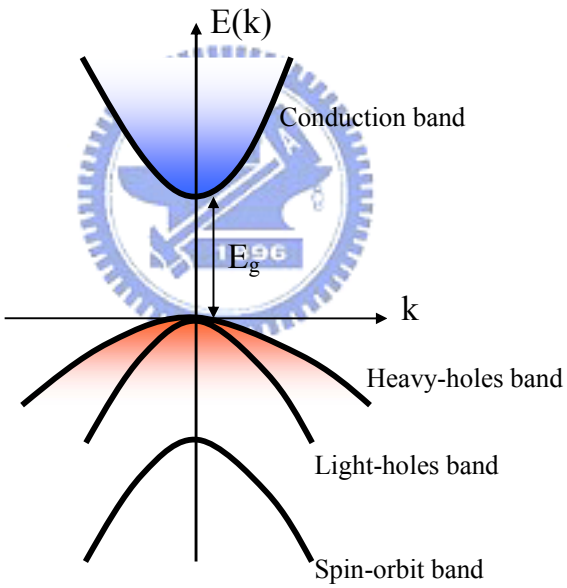

Figure.2.3. Schematic band structure of the direct gap semiconductor using Kane's model. The heavy-hole effective mass is corrected in this figure.

The Kane's model is summarized in Fig. 2.3. The heavy-hole effective mass is corrected in the figure.

2.3 SEMICONDUCTOR HETEROSTRUCTURES AND THE EFFECTIVE MASS THEORY

In the previous section, we assumed the semiconductor crystal is infinite. Practically, useful semiconductor optoelectronic devices usually have small size, and are the combination of several semiconductor materials of different band structures (semiconductor heterostructures). When two semiconductors of different band structures are joint, a heterojunction will then forms. There are three types of heterojunctions possible (Fig. 2.4). Furthermore, semiconductor heterostructures important to optoelectronics such as the double heterostructure (DH) and the quantum well are shown in the Fig. 2.5. DH is used in the early semiconductor lasers before quantum-well lasers are invented.

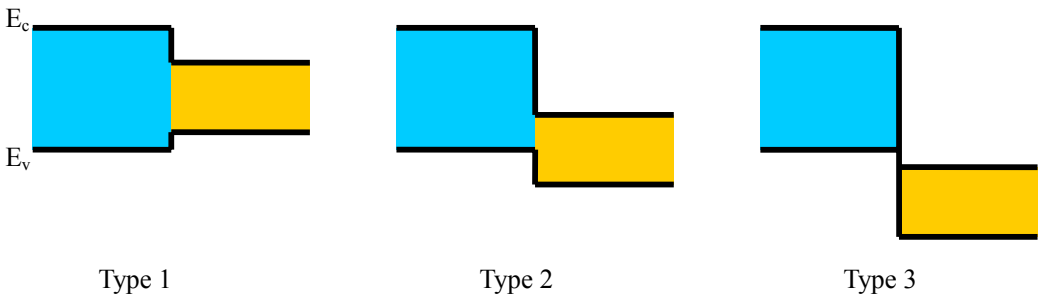

Figure 2.4. Possible three types of semiconductor heterojunctions.

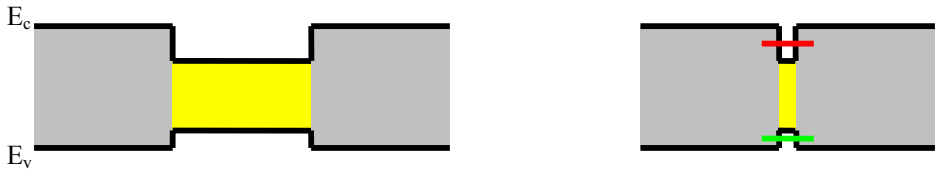

Figure 2.5. Schematic diagrams of the double heterostructure (DH) and the quantum-well heterostructure.

Now, we then need a general theory to describe how an electron behaves in these optoelectronic materials. For the single-band case, the variation of the band stucture with the position can be treated as a perturbation on the Hamiltonian. If this perturbation is slowly varying, then the behavior of an electron in semiconductors can be described as the effective mass theory (EMT) or envelop function approximation (EFA) [3, 14, 15]

$$[-\frac{\hbar^2}{2}\nabla\frac{1}{m^*}\nabla+U(\vec{r})]F(\vec{r})=(E-E_{n,\vec{k}=0})F(\vec{r})\,. \qquad (1.22)$$

where m* is the electron effective mass, U is the perturbation energy function seen by an electron, $E_{n,k=0}$ is the band-edge energy. $F(\vec{r})$ is the envelope function, where $\psi(\vec{r})=F(\vec{r})\cdot u_{n,k=0}(\vec{r})$. Note that (1.22) is very similar to the standard time-independent Schrödinger equation.

For DH, the thickness of the small-band gap region is much larger than the electron's deBroglie wavelength, so the quantum effect is negligible. Classical semiconductor device physics can then be used to analyze the band structure of DH

[3].

For quantum well, the small-band gap region width is comparable to the electron's deBroglie wavelength, and obvious quantum effect will then occur. Theory of the quantum wells will be addressed in the next section.

2.4 QUANTUM WELLS, WIRES, AND DOTS

Low-dimensional structure is an artificial structure that provides one-dimensional to three-dimensional quantum effect. Therefore, the width of the low-dimensional structure and the electron deBroglie wavelength must be in the same order. Because the conduction band effective mass in direct gap semiconductor materials such as InAs and GaAs is usually much smaller than the vacuum electron mass, low-dimensional semiconductor quantum structures have scale in several tens to hundreds of nanometers, rather than the smaller size of a natural atom. We use effective mass theory to accurately describe the behavior of an electron in a low-dimensional semiconductor structures, or semiconductor nanostructures, termed because the electron deBroglie wavelength in a semiconductor is nanoscale.

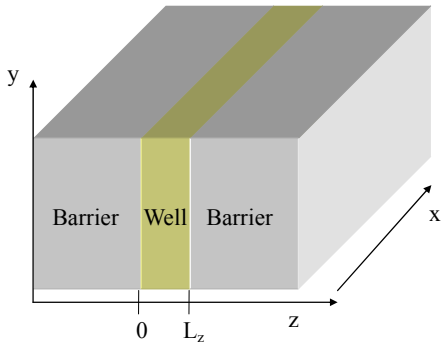

Figure 2.6. Schematic diagram of the quantum well structure.

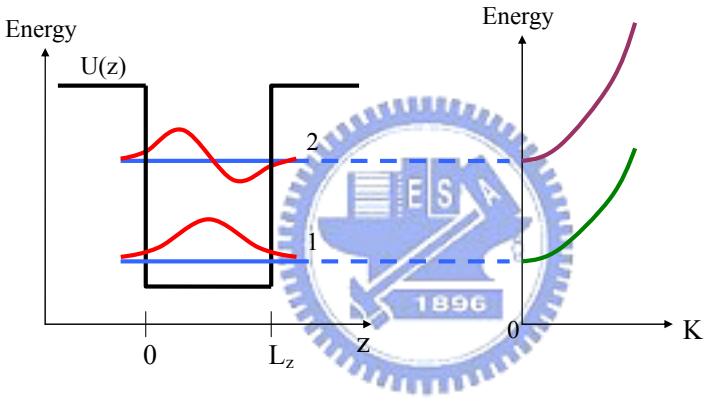

Figure 2.7. Schematic diagram of a quantum well having two energy eigenstates, and the energy spectra in the k-space.

For an electron in an one-dimensional (1D) semiconductor nanostructure, or a quantum well (QW) (Fig. 2.6), the envelope function can be expressed as the product of three components

$$F_{well}(\vec{r}) = e^{i\vec{K}\cdot\vec{R}} \cdot F(z) \tag{1.23}$$

where $\vec{K} = k_x\hat{x} + k_y\hat{y}$, and $\vec{R} = \vec{x} + \vec{y}$. After substitution and assuming the effective

mass is the same in the different materials, the energy eigenvalues of this standard quantum-mechanics problem are

$$E_n = \frac{\hbar^2 \vec{K}^2}{2m_{well}^{*\ 2}} + \varepsilon_n \tag{1.24}$$

where the eigenenergy ε_n satisfies

$$[-\frac{\hbar^2}{2}\frac{\partial}{\partial z}\frac{1}{m^*(z)}\frac{\partial}{\partial z} + U(z)]\,F_n(z) = \varepsilon_n \cdot F_n(z)\,. \tag{1.25}$$

The equation can be solved easily by use of graphical solution method, similar to the rectangular slab waveguide problems. Fig. 2.7 shows schematic of a quantum well having two energy eigenstates, and the energy spectra in the k-space.

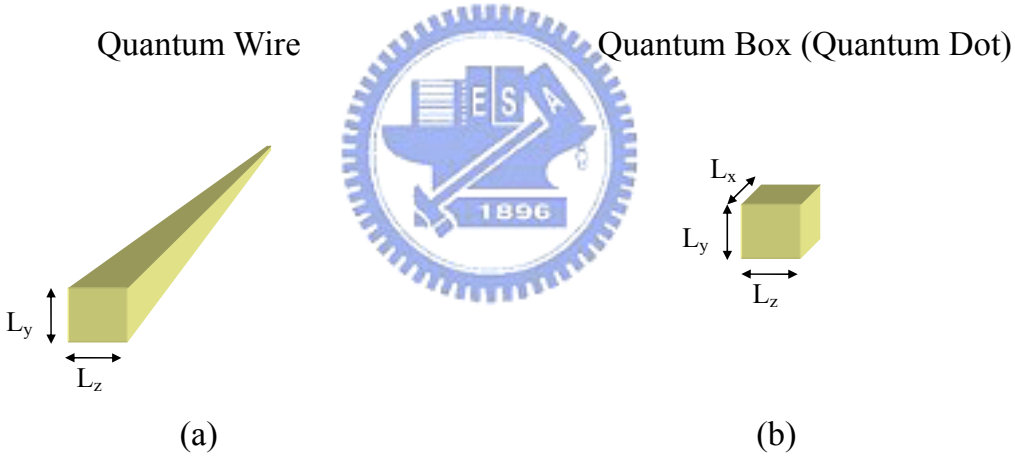

Figure 2.8. Schematic diagrams of (a) quantum wire and (b) quantum dot.

Likewise, quantum wires (Fig. 2.8a) and quantum boxes (or quantum dots, QD) (Fig. 2.8b)are two-dimensional (2D) and three-dimensional (3D) nanostructures, respectively. The effective mass equation can be easily solved using separable variable method.

For quantum wires,

$$F_{wire}(\vec{r}) = e^{ik_x x} \cdot F(y) \cdot F(z) \tag{1.26}$$

$$\mathrm{U}_{\mathrm{wire}}(\vec{\mathrm{r}}) = \mathrm{U}(\mathrm{y}) + \mathrm{U}(\mathrm{z}) \tag{1.27}$$

$$E_n = \frac{\hbar^2 k_x^{\ 2}}{2m_{well}^{*\ 2}} + \varepsilon_n + \varepsilon_m \tag{1.28}$$

$$[-\frac{\hbar^2}{2}\frac{\partial}{\partial \mathrm{z}}\frac{1}{\mathrm{m}^*(\mathrm{z})}\frac{\partial}{\partial \mathrm{z}} + \mathrm{U}(\mathrm{z})]\,\mathrm{F}_{\mathrm{n}}(\mathrm{z}) = \varepsilon_{\mathrm{n}} \cdot \mathrm{F}_{\mathrm{n}}(\mathrm{z}) \tag{1.29}$$

$$[-\frac{\hbar^2}{2}\frac{\partial}{\partial \mathrm{y}}\frac{1}{\mathrm{m}^*(\mathrm{y})}\frac{\partial}{\partial \mathrm{y}} + \mathrm{U}(\mathrm{y})]\,\mathrm{F}_{\mathrm{m}}(\mathrm{y}) = \varepsilon_{\mathrm{m}} \cdot \mathrm{F}_{\mathrm{m}}(\mathrm{y}). \tag{1.30}$$

For quantum boxes,

$$F_{box}(\vec{r}) = F(x) \cdot F(y) \cdot F(z) \tag{1.31}$$

$$\mathrm{U}_{\mathrm{box}}(\vec{\mathrm{r}}) = U(x) + \mathrm{U}(\mathrm{y}) + \mathrm{U}(\mathrm{z}) \tag{1.32}$$

$$E_n = \varepsilon_l + \varepsilon_n + \varepsilon_m \tag{1.33}$$

$$[-\frac{\hbar^2}{2}\frac{\partial}{\partial \mathrm{z}}\frac{1}{\mathrm{m}^*(\mathrm{z})}\frac{\partial}{\partial \mathrm{z}} + \mathrm{U}(\mathrm{z})]\,\mathrm{F}_{\mathrm{n}}(\mathrm{z}) = \varepsilon_{\mathrm{n}} \cdot \mathrm{F}_{\mathrm{n}}(\mathrm{z}) \tag{1.34}$$

$$[-\frac{\hbar^2}{2}\frac{\partial}{\partial \mathrm{y}}\frac{1}{\mathrm{m}^*(\mathrm{y})}\frac{\partial}{\partial \mathrm{y}} + \mathrm{U}(\mathrm{y})]\,\mathrm{F}_{\mathrm{m}}(\mathrm{y}) = \varepsilon_{\mathrm{m}} \cdot \mathrm{F}_{\mathrm{m}}(\mathrm{y}) \tag{1.35}$$

$$[-\frac{\hbar^2}{2}\frac{\partial}{\partial \mathrm{x}}\frac{1}{\mathrm{m}^*(\mathrm{x})}\frac{\partial}{\partial \mathrm{x}} + \mathrm{U}(\mathrm{x})]\,\mathrm{F}_{\mathrm{l}}(\mathrm{x}) = \varepsilon_{\mathrm{l}} \cdot \mathrm{F}_{\mathrm{l}}(\mathrm{x}). \tag{1.36}$$

With the knowledge of the quantum states, it is useful to calculate density of state (D.O.S) D(E), which is defined as the number of quantum states per unit volume between E and $E+dE$. Schematic diagrams of the density of states of bulk materials, quantum wells, quantum wires, and quantum dots are plotted in Fig. 2.9.

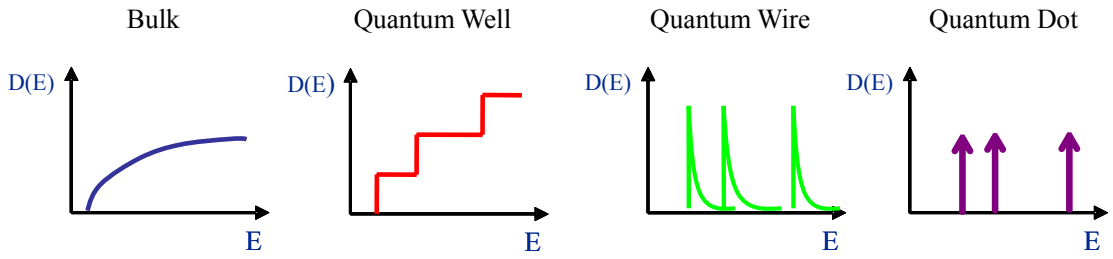

Figure 2.9. Schematic diagrams of the density of states for bulk materials, quantum wells, quantum wires, and quantum dots.

2.5 INTERBAND OPTICAL TRANSITION AND GAIN [2, 3]

We now have a brief review the optical transition in bulk and low-dimensional nanostructures. If the electron-hole system is subjected to a sinusoidal steady-state electromagnetic perturbation (Fig. 2.10), then the optical transition will be possible.

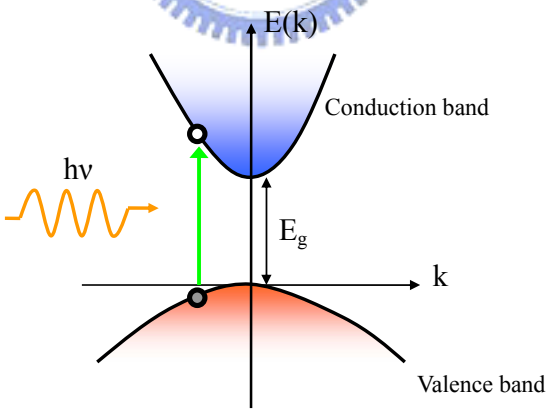

Figure 2.10. Optical interband transition in a direct gap semiconductor material.

In quantum mechanics, time-dependent perturbation theory and the Fermi's golden rule tell us in order to have an optical transition between a state in the conduction

band and a state in the valence band, the transition energy difference must equal to the photon energy ($\Delta E=h\nu$) and the k-selection rule must be obeyed ($k_c \approx k_v$). The transition probability, or transition rate, is proportional to the optical matrix element

$$H'_{ba} = \langle b | -e\vec{r} \cdot \vec{E} | a \rangle \tag{1.37}$$

where a and b denote the wave function of the two states. Using slowly-varying approximation and the Bloch theorem, we can have

$$\langle b | -e\vec{r} \cdot \vec{E} | a \rangle \cong -\frac{eA_0}{2m_0} \hat{e} \cdot \vec{P}_{cv} \cdot \delta_{k_c, k_v} \tag{1.38}$$

where P_{cv} is the interband momentum matrix element, $\hat{e}$ is the unit directional vector of the electric field and A0 is the amplitude of the vector potential.

The gain coefficient g is defined as the fraction of photons increased per unit distance:

$$g = \frac{1}{S}\frac{dS(z)}{dz} = \frac{1}{I}\frac{dI(z)}{dz} \tag{1.39}$$

where S is the photon density and I is the light intensity.

For a bulk semiconductor, assuming the conduction band is completely empty, and the valence band is completely full, then gain coefficient of the bulk semiconductor is

$$g_{bulk}(h\nu) = \frac{\pi e^2}{n_r c \varepsilon_0 m_0^2 \omega} \cdot \left| \hat{e} \cdot \vec{P}cv \right|^2 \cdot D_r(h\nu - E_g) \cdot (f_c - f_v) \tag{1.40}$$

where fc and fv are the Fermi-Dirac distribution for the electronic state and hole state, respectively. Dr is the density of state using the reduced effective mass

$$\frac{1}{m_r} = \frac{1}{m_e^*} + \frac{1}{m_h^*}. \tag{1.41}$$

Note that the gain coefficient is positive if fc>fv (population inversion). At this time,

the light in the material will be amplified.

For a low-dimensional semiconductor nanostructure, and assuming the valence band-mixing effect is negligible, and there is only one quantized state in each of the conduction and valence band, the gain coefficient is

$$g_{\text{low-dimensional}}(h\nu) = \frac{\pi e^2}{n_r c \varepsilon_0 m_0^2 \omega} \cdot \left|I_h^e\right|^2 \left|\hat{e} \cdot \vec{P}cv\right|^2 \cdot D_r^l(h\nu - E_g) \cdot H(h\nu - E_{hm}^{en}) \cdot (f_c - f_v) \tag{1.42}$$

where

$$E_h^e = E_g + E_e - E_h \tag{1.43}$$

is the interband transition energy. Because the density of states spectra of the low-dimensional nanostructures is sharper and higher than that of the bulk semiconductors, the max gain achievable where lasing behavior usually occur is higher in low-dimensional nanostructures than in bulk materials. This characteristic opens the applications of the low-dimensional nanostructures in optoelectronics, termed “nano-photonics”.

2.6 SEMICONDUCTOR LASERS [1, 2]

Semiconductor lasers are important optoelectronic devices. Applications of the semiconductor lasers include optical storage, optical communication, medical use etc. Before we discuss how semiconductor lasers can be used to slow down optical information velocity, it is beneficial to have a brief review on the basic properties of the Fabry-Perot resonators.

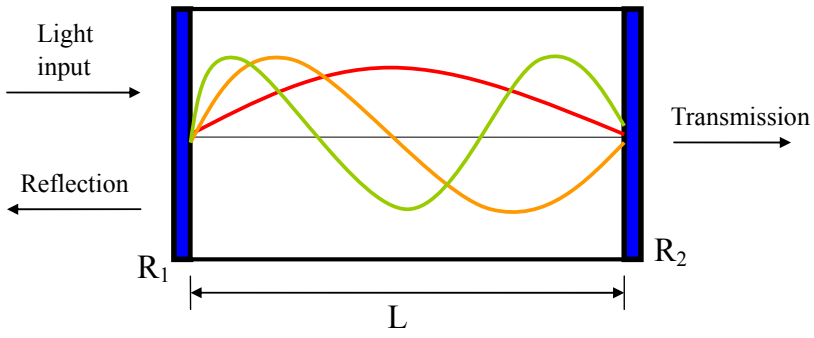

Figure 2.11. Schematic illustration of a Fabry-Perot resonator with mirror reflectivity R_1 and R_2.

A Fabry-Perot resonator (Fig. 2.11) consists of two planar mirrors of reflectivity R1 and R2. Assuming lossless mirrors and no mirror phase shift, the electric field transmission coefficient t and the electric field reflection coefficient r of the Fabry-Perot resonator are as follow [1]:

$$t = \frac{t_1 \cdot t_2' \cdot \exp[-i\frac{2\pi nL}{\lambda_0}]}{1 - r_1' \cdot r_2' \cdot \exp[-i\frac{4\pi nL}{\lambda_0}]} \tag{1.44}$$

$$r = \frac{r_1 + r_2' \cdot \exp[-i\frac{2\pi nL}{\lambda_0}]}{1 - r_1' \cdot r_2' \cdot \exp[-i\frac{4\pi nL}{\lambda_0}]} \tag{1.45}$$

where r_1, r_1', r_2, r_2', t_1, t_1', t_2, t_2' are reflection and transmission coefficients of the mirrors. The intensity transmission coefficient T and the intensity reflection coefficient R of the Fabry-Perot resonator are defined as the square of the absolute value of t and r, respectively.

From (1.44), the t is unity if

$$2L = m \cdot \frac{\lambda_0}{n} \tag{1.46}$$

where m is any integer. On the other hand, r is zero also whenever

$$2L = m \cdot \frac{\lambda_0}{n}. \tag{1.47}$$

Optical wavelengths fulfilling this resonant condition are called Fabry-Perot cavity modes. It is worthwhile noting that the condition t=1 and r=0 is the resonant transportation of the photon, which has its counterpart in the electronic device examples. Furthermore, the phase of the t and r has its profound significance for use in slowing light information speed, which will be addressed in the next chapter of the thesis.

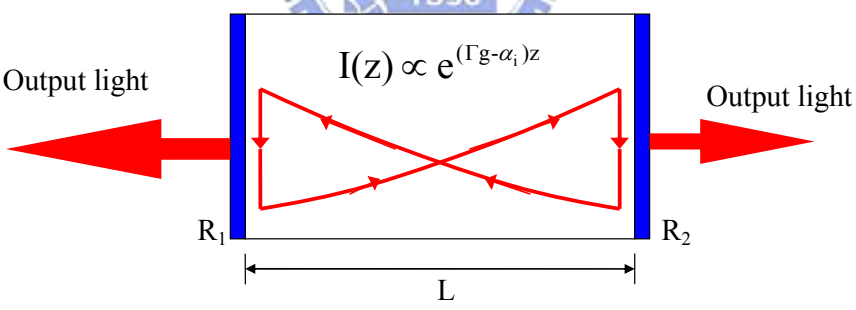

Figure 2.12. Schematic diagram of an asymmetric Fabry-Perot resonator with a gain material.

If the resonator includes a gain material (An active resonator), then the story will be more interesting. Fig. 2.12 shows schematic of an asymmetric Fabry-Perot resonator with a gain material. The electric field transmission coefficient becomes

$$t = \frac{t_1 \cdot t_2' \cdot \exp[-i\frac{2\pi mL}{\lambda_0}] \cdot \exp[\frac{(\Gamma g - \alpha_i)}{2} L]}{1 - r_1' \cdot r_2' \cdot \exp[-i\frac{4\pi mL}{\lambda_0}] \cdot \exp[(\Gamma g - \alpha_i) L]} \tag{1.48}$$

According to (1.48), t will be infinite if

$$\Gamma g_{th} = \alpha_i + \alpha_m = \alpha_i + \frac{1}{2L} \ln\left(\frac{1}{R_1 R_2}\right) \quad \text{Gain condition} \tag{1.49}$$

and

$$2L = m \cdot \frac{\lambda_0}{n} \quad \text{Phase condition} \tag{1.50}$$

where Γ is the optical confinement factor. (1.49) is the threshold condition of the lasers. When above threshold, the gain coefficient of the gain material will clamp at the threshold value because of the mechanism of gain saturation [1, 2]. Extra carriers will rapidly recombine and produce photons in the lasing cavity mode.

In a semiconductor laser, electrons in conduction band and holes in valence band can recombine and produce photon emission. In order to control flow of the carriers, a forward biased p-n junction is generally used in a semiconductor laser. Besides, optical waveguides are needed in order to provide optical confinement and hence can reduce optical loss. In a double heterostructure (DH) semiconductor laser (Fig. 2.13), the central GaAs region provides both the carrier confinement and optical confinement because of the conduction and valence-band profiles and the refraction index profile [3].

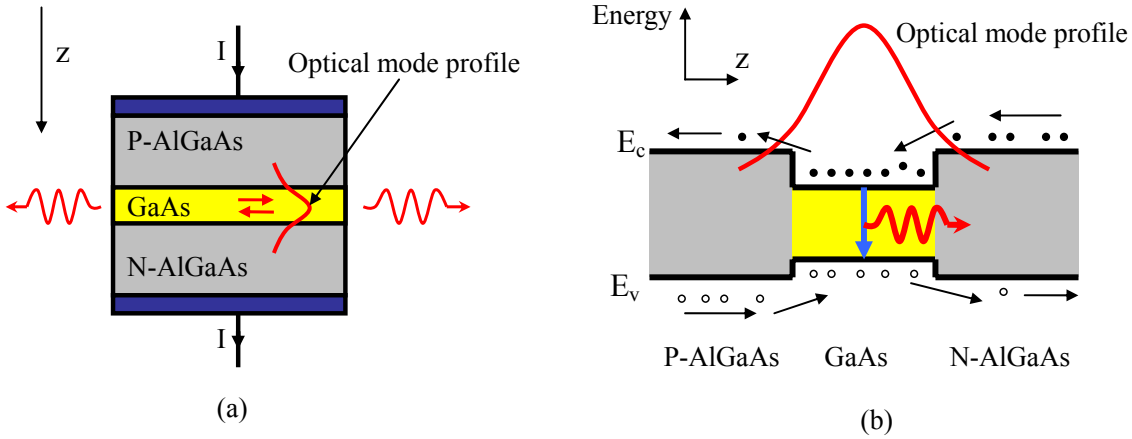

Figure 2.13. (a) A double heterostructure (DH) semiconductor laser and (b) its band structure profile.

Light output power of semiconductor lasers when above its lasing threshold can be shown as

$$P_{out} = \frac{h\nu}{e}\frac{\alpha_m}{\alpha_i + \alpha_m}\cdot\eta_i\cdot(I - I_{th}) \tag{1.51a}$$

where η_i is the internal quantum efficient, defined as the percentage of the injected carriers that contribute to the radiative recombination. The external quantum efficiency η_e is defined as

$$\eta_e = \frac{\frac{dP_{out}}{dI}}{\frac{h\nu}{e}} = \eta_i \frac{\frac{1}{L}\ln(\frac{1}{R})}{\alpha_i + \frac{1}{L}\ln(\frac{1}{R})}. \tag{1.51b}$$

Fig. 2.14 shows schematic diagram of the light power–injection current curve (L-I curve) of a semiconductor laser.

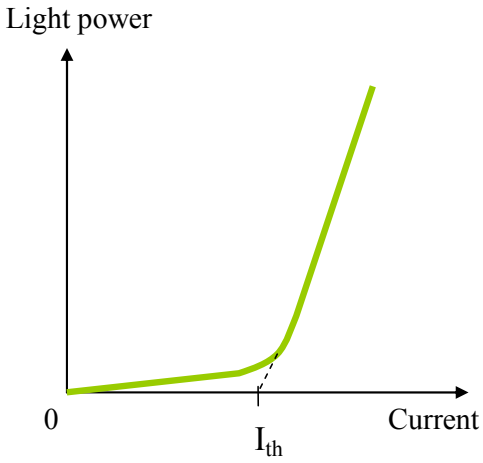

Figure 2.14. Schematic diagram of the light power–injection current curve (L-I curve) of a semiconductor laser.

Free spectrum range (FSR) of the Fabry-Perot resonator is defined as the separation between neighboring cavity modes in the frequency spectrum, or

$$FSR = \nu_{m+1} - \nu_m = \frac{c}{2nL}. \tag{1.52}$$

In order to have a single-frequency laser, FSR need to be large enough compared with gain spectrum. According to (1.52), to have large FSR, the cavity length L must be small. Compared with the long cavity length of a edge-emitting semiconductor laser such as the double heterostructure semiconductor lasers and the quantum-well Fabry-Perot lasers, vertical-cavity surface-emitting lasers (VCSELs) (Fig. 2.15) have cavity length of several optical wavelength. Thus, VCSEL is an ideal candidate for the single frequency semiconductor lasers. Fig. 2.16 shows the cavity mode spectra for edge-emitting laser (EEL) and VCSEL, and optical gain spectra against frequency.

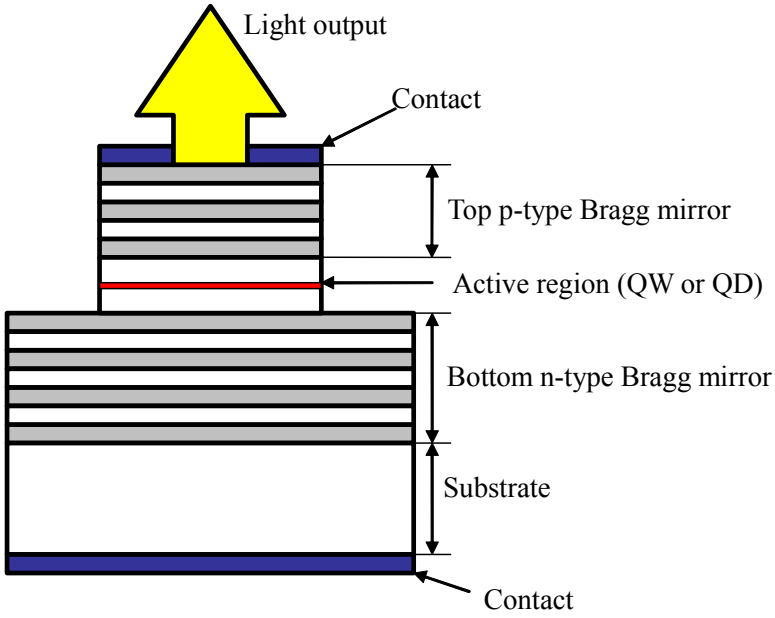

Figure 2.15. Device structure of VCSEL.

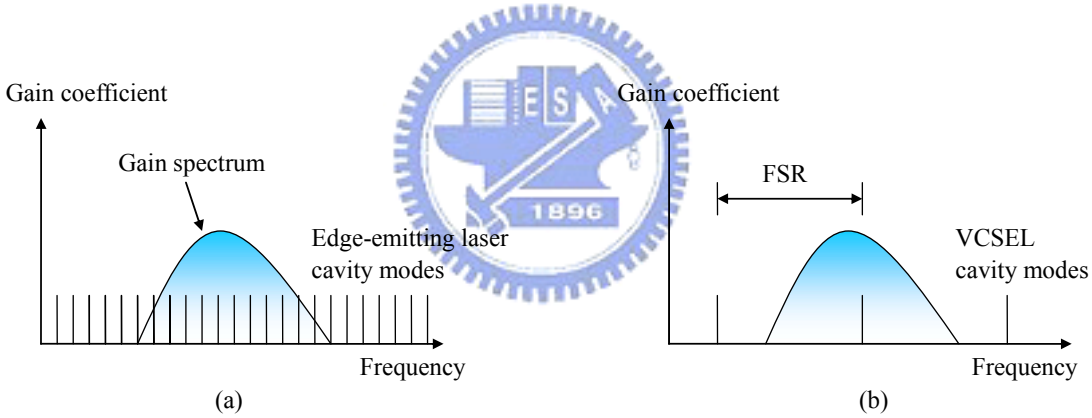

Figure 2.16. Cavity mode spectra for (a) edge-emitting laser and (b) VCSEL, and optical gain spectra against frequency.

However, because short cavity length induces large mirror loss, making high-reflectivity laser mirrors and then decreasing mirror loss becomes a critical issue of VCSEL. Distributed Bragg reflectors (DBRs) consist of alternating layers of dielectric or semiconductor materials. The difference in the index of refraction

between adjacent layers give rise to a high reflectivity (>99%) at the vicinity of the Bragg frequency [1]. The thickness of each layer is $\lambda_0/(4n)$, where n is the index of refraction of the layer [1]. At the Bragg wavelength, the reflectivity of the DBR is given by [16]:

$$R_{DBR}^{max} = \left(\frac{1 - \left(\frac{n_L}{n_H} \right)^{2p}}{1 + \left(\frac{n_L}{n_H} \right)^{2p}} \right)^2 \tag{1.53}$$

where p is the number of the quarter-wave pairs. n_H is the larger refraction index, while n_L stands for the smaller one. The reflectivity spectra of the DBRs can be calculated using transfer matrix method. Fig. 2.17 shows the calculated reflectivity spectra of the DBRs with different number of quarter-wave pairs.

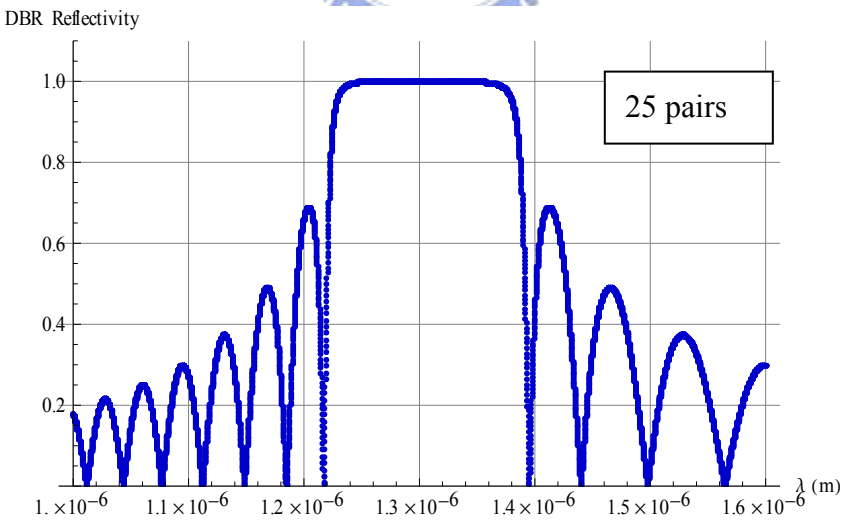

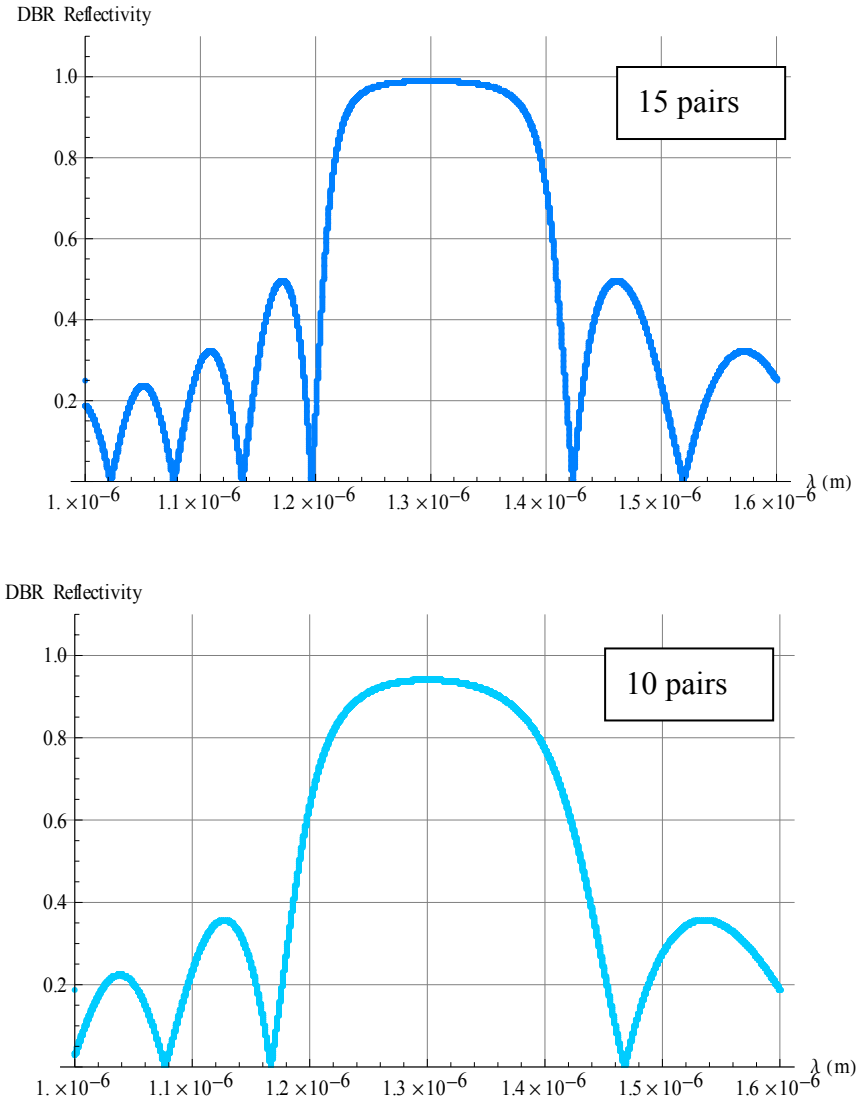

Figure 2.17. Calculated reflectivity spectra of the $Al_{0.9}Ga_{0.1}As/GaAs$ DBR ($\lambda_{Bragg} = 1300$ nm) with different number of quarter-wave pairs.

2.7 HIGH-SPEED DIRECT MODULATION OF SEMICONDUCTOR LASERS [1-3]

Optical communication is one of the most important applications of the semiconductor lasers. A unique feature of semiconductor lasers is that, unlike other lasers that are modulated externally, the semiconductor laser can be modulated

directly by modulating the injection current [1]. This is especially important in view of the possibility of monolithic integration of the two principle actors of the modern information era—the transistor and the laser—in integrated semiconductor optoelectronic circuits [1].

Light output power of the Semiconductor lasers is proportional to ($I-I_{th}$). Therefore, if the injection current has a dc component and a small signal sinusoidal modulation:

$$I(t) = I_0 + i(t) = I_0 + i_m(\omega)e^{j\omega t} \quad \text{(Current)} \tag{1.54}$$

$$J(t) = J_0 + j(t) = J_0 + j_m(\omega)e^{j\omega t} \quad \text{(Current density)} \tag{1.55}$$

$$N(t) = N_0 + n(t) = N_0 + n_m(\omega)e^{j\omega t} \quad \text{(Carrier density)} \tag{1.56}$$

then we would expect that the light output power will correspondingly be with a dc component and a small signal sinusoidal modulation terms

$$P(t) = P_0 + p(t) = P_0 + p_m(\omega)e^{j\omega t} \quad \text{(Light output power)} \tag{1.57}$$

$$S(t) = S_0 + s(t) = S_0 + s_m(\omega)e^{j\omega t} \quad \text{(Photon density).} \tag{1.58}$$

Then we can transform electrical signal into optical format (Fig. 2.18)by use of semiconductor lasers, and then transmit information optically.

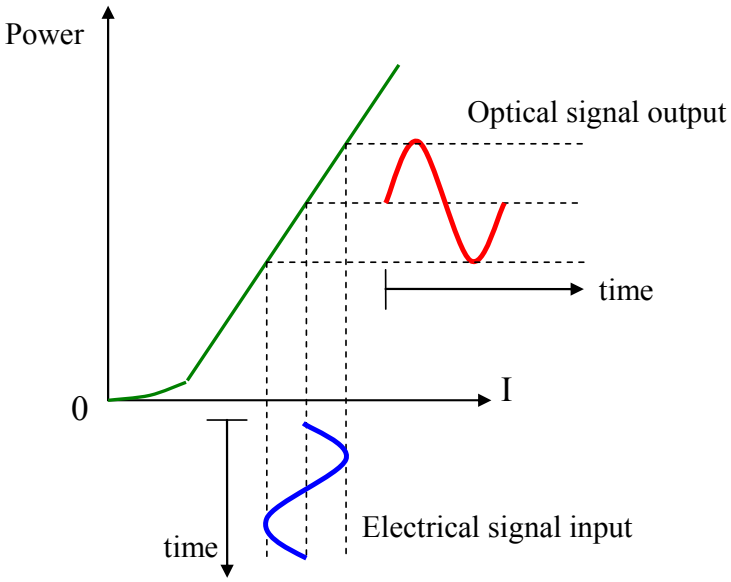

Figure 2.18. Schematic diagram of the direct modulation of semiconductor lasers.

To have a review on the basic theory of the direct modulation of semiconductor lasers, let us start from the carrier density (N) and photon density (S) rate equation:

$$\frac{dN}{dt} = \frac{J}{ed} - v \cdot g(N) \cdot S - \frac{N}{\tau} \tag{1.59}$$

$$\frac{dS}{dt} = \Gamma \cdot v \cdot g(n) \cdot S - \frac{S}{\tau_p} + \beta_{sp} R_{sp} \tag{1.60}$$

Where β_{sp} is the spontaneous emission factor, τ is the carrier lifetime, and R_{sp} is the spontaneous emission rate per unit volume. τ_p is the photon lifetime

$$\frac{1}{\tau_p} = \left(\frac{c}{n_r}\right) \cdot \left[\alpha_i + \frac{1}{2L} \ln\left(\frac{1}{R_1 R_2}\right)\right]. \tag{1.61}$$

Assuming there is only one lasing mode, and using linear gain approximation

$$g(N) = g_0 + g'(N - N_0) \tag{1.62}$$

Where g' is the differential gain at $I=I_0$, in addition to small Signal approximation:

$$J_0 >> J_m$$

$$N_0 >> n_m \tag{1.63}$$

$$S_0 >> s_m$$

, then it can be shown that

$$\mathrm{s}_m(\omega) = \left[\frac{\Gamma \tau_p \omega_r^2}{-j\omega(\frac{1}{\tau} + S_0 \cdot v \cdot g') - \omega^2 + \omega_r^2} \right] \cdot \left(\frac{j_m(\omega)}{ed} \right) \tag{1.64}$$

where

$$\omega_r^2 = vg' \left(\frac{\mathrm{S}_0}{\tau_p} \right). \tag{1.65}$$

And

$$f_r = \frac{\omega_r}{2\pi} = \frac{1}{2\pi} \sqrt{v \cdot \left(\frac{\partial g}{\partial N} \right)_{N_0} \cdot \left(\frac{S_0}{\tau_p} \right)} \tag{1.66}$$

is the relaxation frequency. Modulation frequency response $M(\omega)$ is:

$$M(\omega) = \left| \frac{\mathrm{s}_m(\omega)}{\mathrm{j}_m(\omega)} \right| = \left| \frac{\frac{\Gamma \tau_p \omega_r^2}{\mathrm{ed}}}{j\omega(\frac{1}{\tau} + S_0 \cdot v \cdot g') - \omega^2 + \omega_r^2} \right| = \frac{\Gamma \tau_p}{\mathrm{ed}} \frac{\omega_r^2}{\left[\omega^2 (\frac{1}{\tau} + S_0 \cdot v \cdot g')^2 - (\omega^2 - \omega_r^2)^2 \right]^{1/2}} \tag{1.67}$$

which peaks at $\omega = \omega_{\mathrm{r}}$.

Given that the photon lifetime in a typical semiconductor laser is about several pico-seconds, differential gain is of the order of $10^{-6} cm^2$, photon density is about $10^{15}\ photons/cm^3$, the modulation frequency or modulation bandwidth is about

several GHz. The high-speed modulation ability and the compact volume make semiconductor lasers an ideal candidate for signal transmitter in optical electronics.

Increasing injection current increases the light output, and then increases the relaxation frequency. Fig. 2.19 shows schematic plot of modulation spectra at different injection currents.

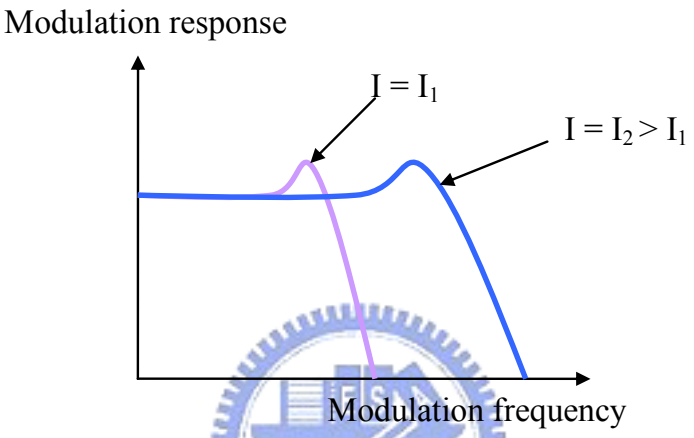

Figure 2.19. Schematic plot of the modulation spectra of a semiconductor laser at different injection currents.

A very important concept, but people are usually ignorant, is that the optical spectrum of a modulated single-frequency semiconductor laser is not longer single-frequency. When subjected to a sinusoidal direct modulation, the photon number in the laser cavity and the light output power is modulated. Hence, the amplitude of the electric field of the laser light is also modulated. This is the amplitude modulation (AM) scheme. The electric field under AM can be easily shown [17]:

$$E(t) = E_0(1 + m\sin[\omega_m t])\sin[\omega_c t]$$

$$= E_0 \sin[\omega_c t] + \frac{m}{2} E_0 \cos[(\omega_c - \omega_m)t] - \frac{m}{2} E_0 \cos[(\omega_c + \omega_m)t] \quad (1.68)$$

Where m is the modulation index, ω_c is the carrier frequency, and ω_m is the modulation frequency. Schematic optical spectra of the direct modulated single-frequency laser are shown in the Fig. 2.20.

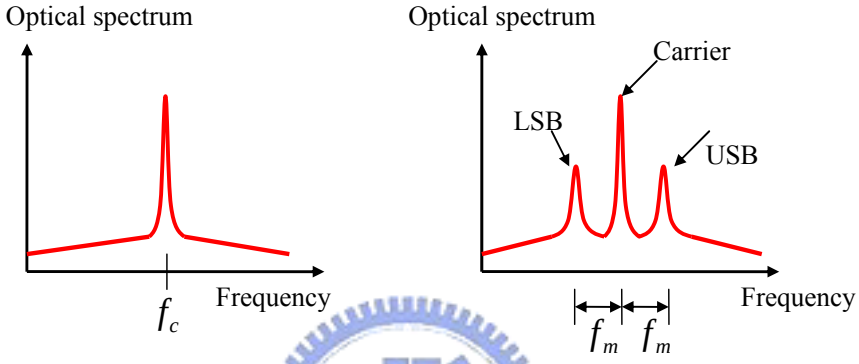

Figure 2.20. Schematic optical spectra of a single-frequency semiconductor laser and a direct modulated single-frequency laser.

(LSB: Lower side band. USB: upper side band, f_m: modulation frequency, f_c: carrier frequency)

2.8 SEMICONDUCTOR LASERS WITH LOW-DIMENSIONAL GAIN MATERIALS

A semiconductor laser with low-dimensional gain materials is superior to its counterpart with bulk gain materials, or double-heterostructure (DH) lasers.

Because of the discrete energy eigenstates, gain spectra of the low-dimensional nanostructures are narrower than bulk materials. As a result, injected carriers can

effectively increase the population inversion within a narrower spectra width. This characteristic makes lasers with low-dimensional gain material can have larger differential gain and smaller threshold current densities than conventional DH semiconductor lasers. Thus, lasers with low-dimensional gain material can have larger modulation relaxation frequency and larger available modulation bandwidth as compared with DH lasers. Compared with QW gain materials, ideal QD have very sharp density of states. The gain spectrum of an ideal QD material is narrowly centered on its transition energy. Therefore, based on the laser theory, it is easier and quicker to reach threshold gain in an ideal QD laser than in an ideal QW laser. Besides, the lasing wavelength of the lasers with low-dimensional gain material is less sensitive to the injection current, because of the narrower gain spectra. Fig. 2.21 shows schematic plots of the gain spectra of the ideal QW and QD lasers.

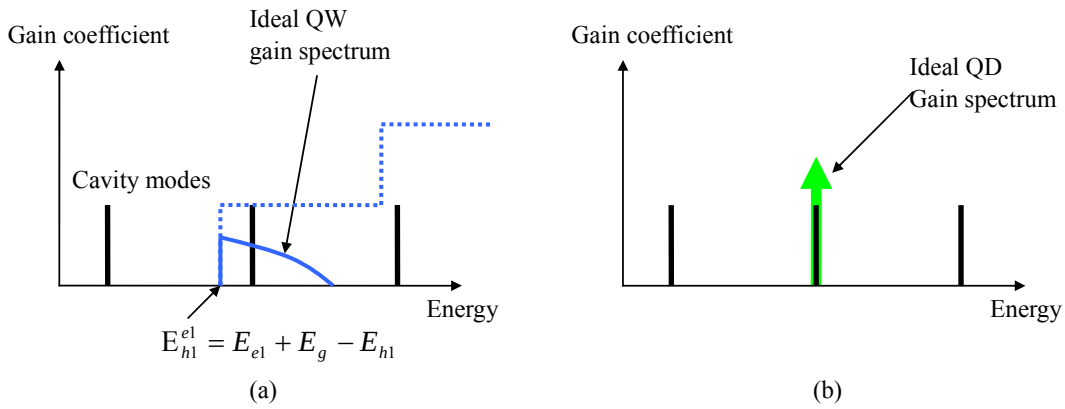

Figure 2.21. Schematic gain spectra of ideal (a) QW laser and (b) QD lasers.

Modern crystal growth techniques such as the molecular beam epitaxy (MBE) and the metal-organic chemical vapor deposition (MOCVD), has demonstrated that it is

possible to grow semiconductors of different atomic compositions on top of another semiconductor substrate with monolayer precision [3]. Therefore, high-quality quantum-well gain materials can be made by utilizing these epitaxy techniques.

Since the mid-1990s, there has been considerable work on the direct synthesis of semiconductor nanostructures by applying the phenomenon of island formation during strained-layer heteroepitaxy, a process called the Stranski-Krastanow growth mode [16]. During the heteroepitaxial growth, the semiconductor atoms tend to form islands spontaneously on a planar wetting layer because the strain energy can be relaxed and is energetically favorable there. If these islands are small enough to have quantum effect, they are called self-assembled quantum dots.

Due to the much higher number of available states in the 2-D wetting layer and barrier states at high temperatures, compared to that in the dots, injected carriers preferably occupy the wetting layer and barrier states [18]. This makes the carrier dynamics of the real quantum dots dependent not only on the QD discrete levels, but also on the wetting layer and barrier states. Besides, the QD size non-uniformity during the spontaneous self-organized process can causes the ground-state (GS) optical transition energies of the quantum dots vary from one QD to another and hence broaden the gain spectrum, so the real GS optical gain spectrum of QD is not an ideal delta function. These difficulties limit the performances of today's QD lasers.

In the thesis, we will study the slow-light phenomenon in a self-organized QD laser, whose QD active region is fabricated by use of MBE technique.

2.9 SUMMARY

In this chapter, the basic theory of the semiconductor band structures using Kane's $k \cdot p$ model and the low-dimensional nanostructures is reviewed. Subsequently, electron-photon interaction in semiconductors and its low-dimensional structures is described using semi-classical approach. Then we review the basics of semiconductor lasers. Finally, semiconductor lasers with low-dimensional gain materials and their challenges are discussed.

Chapter 3

SLOWING LIGHT USING QUANTUM-DOT LASER AMPLIFIERS

3-1 INTRODUCTION [1, 8-11, 19-34]

The reduction in light group velocity, termed "slow light", has been a fast-moving topic recently, with potential applications from quantum computing to communications [19]. Before the study of the slow-light using semiconductor lasers, a brief review of the important definitions and terms would be helpful.

Referring to Fig. 3.1, we consider the transmission of an input light signal x(t) through a general photonic system, and the output light signal is y(t).

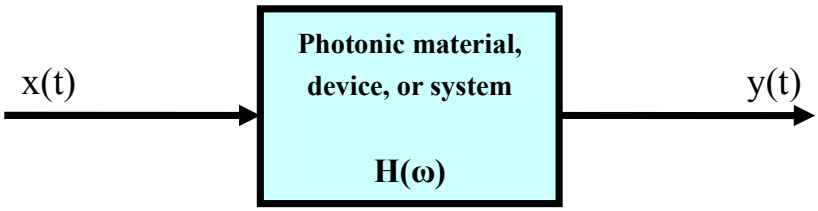

Figure 3.1. Schematic drawing of a general photonic transmission system. The box can be an atomic medium, a semiconductor quantum-dot nanostructure, an optoelectronic device, and so on.

If the photonic "box" is a linear time-invariant system, in the frequency domain, the output Fourier transform Y(t) is the product of the input Fourier transform X(t) and the frequency response of the photonic "box", and this relationship can be written

$$Y(\omega) = H(\omega) \cdot X(\omega) \tag{3.1}$$

Typically H(ω) is complex, which we will write as $H(\omega) = |H(\omega)| \cdot e^{-i\phi(\omega)}$, where $|H(\omega)|$ is the amplitude response and $\phi(\omega)$ is the phase response. If the amplitude response is uniform over the optical regime of the input light signal and the higher-order terms in phase response can be neglected, the output signal remains identical to that of the input signal, with a time delay of $(d\phi / d\omega)$. Thus the propagation time delay, referred to as the group delay, due to propagation through the photonic box plotted in Fig. 3.1 is given by

$$\tau = \frac{d\phi}{d\omega} \tag{3.2}$$

which is, in general, a function of frequency. If the physical length of the photonic box is L, then the group velocity in the box can be defined

$$v_g = \frac{L}{\tau}. \tag{3.3}$$

Besides, the slowdown factor S is

$$S = \frac{c}{v_g} \tag{3.4}$$

which is equivalent to the definition of the group index n_g.

3.1.1 Slowing Light with Material Dispersion

When the photonic box is an optical material, we have

$$\phi(\omega) = \frac{\omega}{c} n(\omega) \cdot L \,. \tag{3.5}$$

Here, n(ω) is the frequency-dependent refraction index of the material, and L is the length of the material. Applying (3.2), we find that

$$\tau = \frac{L}{c / n_g} \tag{3.6}$$

where group index $n_g = n(\omega) + \omega \frac{dn}{d\omega}$ in this case. So the group velocity of the light signal in the photonic material can be written

$$v_g = \frac{L}{\tau} = \frac{c}{n(\omega) + \omega \frac{dn}{d\omega}} \tag{3.7}$$

To obtain a very slow light group velocity, we can increase the material index n(ω) and/or the material dispersion $\frac{dn}{d\omega}$. However, it is hard to change the material index, because it is related to the inherent absorption/gain spectra by the famous Kramer-Kronig relation. Though producing a sharp dip in the gain/absorption spectra, the material dispersion can be very large, based on Kramer-Kronig relation.

Various mechanisms have been used to obtain a large material dispersion for achieving slow light [8, 9, 21]. These include electromagnetically induced transparency (EIT) [22, 23], coherent population oscillations (CPOs) or four-wave mixing (FWM) in atomic crystals [24] and semiconductor optical amplifiers [25-29], etc.

While having a very large slowdown factor, EIT needs a long dephasing time, so that the quantum coherent interference between the quantum energy levels is not destroyed. This makes EIT impossible to be achieved at room temperature. Compared with EIT, CPO is less sensitive to the dephasing effect, so it may be used as the basis of the room-temperature slow-light devices. To increase the bandwidth in a CPO medium, semiconductor-based materials has been proposed because of its longer carrier lifetime (~1 ns) than atomic crystals (~ms). With the discrete energy levels and the stronger carrier confinement, recent experiments have been successful using CPO or FWM in QW and QD devices from low to room temperatures [27-29].

3.1.2 Slowing Light with Waveguide Dispersion and Optical Resonators

In addition to material dispersion, slow-light can also be achieved by utilizing structurally dispersive resonators. Recently, group delay of 110-140 ps of a 200 MHz sinusoidal signal in a coupled ring optical waveguide (CROW) has been experimentally demonstrated [30]. However, the delay in a passive CROW or a passive resonator is not tunable. Chuang et al varied the group delay by changing the injection current of a quantum-well Fabry-Perot laser amplifier [10] and a semiconductor DFB-phase-shifted coupled cavity [31, 32]. Besides, slowing light using photonic crystal defect cavities has also been experimentally demonstrated [33].

In addition the experiment, designing of a resonator slow light device is an interesting issue. Designing coupled-resonator optical waveguide delay line has

been proposed using transfer matrix, tight-binding, and time domain formalisms, and these points of view are consistent with one another [34]. Among these theoretical analysis tool, transfer matrix approach is particularly enabling because it can deal with any arbitrary sequence of resonator [34]. On the other hand, Chuang et al uses transfer matrix method to analyze the phase response of the coupled cavity under various current injection [31, 32]. With this information, they can predict group delay of a sinusoidal signal, and then reshape the waveform of the delayed pulse train. These successful designing tools largely increase the practicability of the slow light devices with dispersive resonators.

3.1.3 Applicability and Design Issues of Slow-Light Devices [11, 31, 32]

While both material and structurally dispersive method offer unique features, it is important to evaluate them in terms of their applicability to delay line.

For a practical tunable optical delay line, one would require [31, 32]

1. Continuously tunable group delay via an external control mechanism, which may be electrical, optical, or even mechanical.
2. Minimal power variation accompanying change in delay
3. Of useful bandwidth. This is the key towards implementations of compact optical delay line because broadband signals in the GHz-range are required in most communications applications [11].
4. Compactness and suitability to integration into optoelectronic platforms.

5. Room-temperature operation.

3.2 REVIEW OF THE PREVIOUS EXPERIMENTAL WORK [12]

3.2.1 QD-Laser Device Structure [12, 35]

The device used in this study is a quantum-dot vertical-cavity surface-emitting laser (QD-VCSEL) and is depicted in Fig. 3.2.

The device structures were fabricated using molecular beam epitaxy (MBE) by NL Nanosemiconductor GmbH (Germany), grown on (100) plane of the GaAs substrates. The top mirror is a 22-pair carbon-doped p^+-$Al_{0.9}Ga_{0.1}As$/p^+-GaAs distributed Bragg reflector (DBR), and the bottom mirror is a 33.5-pair Si-doped n^+-$Al_{0.9}Ga_{0.1}As$/n^+-GaAs DBR. In order to increase the electrical conductivity of DBRs, Carbon and Silicon of relatively high concentration about $2\text{-}3\times10^{18}$ cm^{-3} is used as the p-type dopant in the top DBR and n-type dopant in the bottom DBR respectively, which can result in absorption in the DBRs and hence limit the maximum achievable mirror reflectivity.

The length of the undoped graded-index separate confinement heterostructure (GRINSCH) optical cavity was 3λ, without taking DBR penetration depths into account.

The active region is composed of five quantum-dot groups. Each group has three layers of quantum dots, and is located within the locations of the intracavity intensity distribution maximum, inset between two linear-graded $Al_xGa_{1-x}As$ (x = 0 to 0.9 and x

= 0.9 to 0) confinement layers. The light-current curve of the QD-VCSEL is shown in Fig. 2.3. The details of the device structure were described in [35].

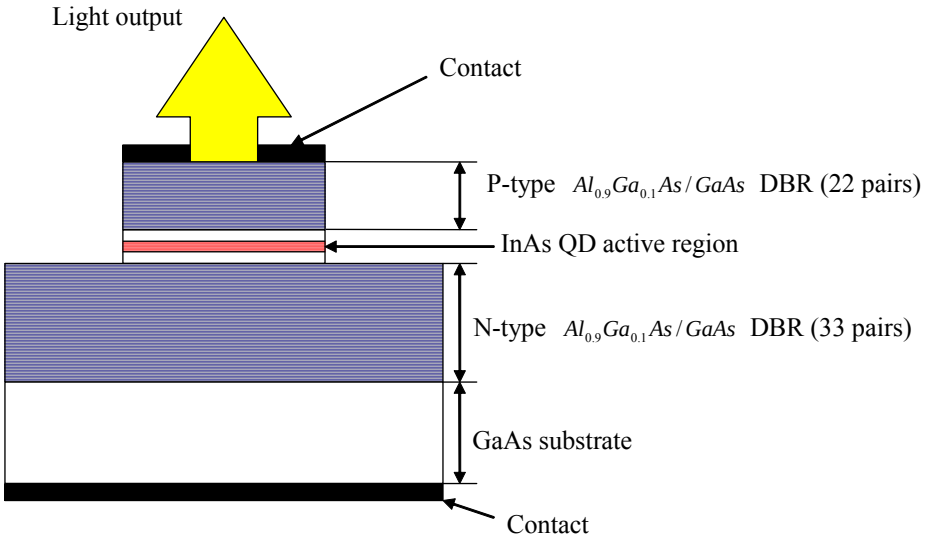

Figure 3.2. Schematic diagram of the QD-VCSEL.

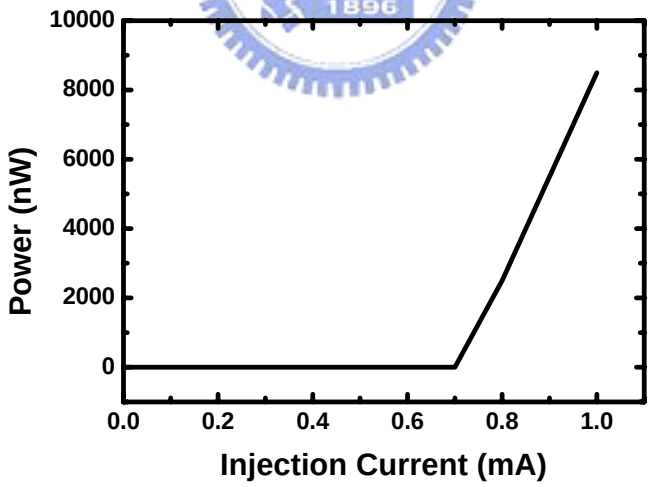

Figure 3.3. Light power-injection current curve of the QD-VCSEL [12].

3.2.2 Experimental Setup

Our experimental setup for optical delay measurement is shown in Fig. 3.4.

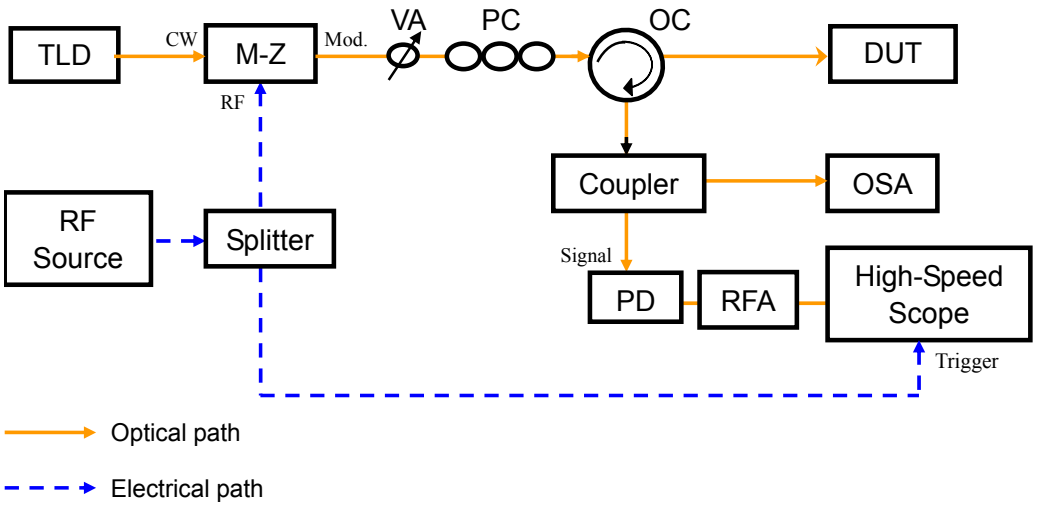

Figure 3.4. Experimental setup used for group delay measurement.

(TLD: tunable laser diode; VA: variable attenuator; PC: polarization controller; OC: optical circulator; OSA: optical spectrum analyzer; PD: photodetector; RFA: RF amplifier; DUT: device under test, which is the QD-VCSEL in this study).

The 1300-nm tunable laser diode produces the continuous-wave (CW) probe light. A sinusoidal light signal is then generated after the CW probe light is sent through a Mach-Zehnder interferometric waveguide electro-optical modulator [1-3], which is driven by an RF source. A variable optical attenuator is used to control the power of the light signal, which is fixed to -14 dBm (~40 μW) in this study. A polarization controller (PC) is used to adjust the polarization of the input light signal. The carrier frequency of the input light signal is adjusted to the QD-VCSEL resonance frequency. The resonance wavelength of the QD-VCSEL is determined by observing directly on

the optical spectrum analyzer (OSA). We measure the signal group delays by estimating the scope traces directly. The group delay reference was taken for an input light signal well away from the QD-VCSEL resonance, which is logical because the reflective phase response is flat.

3.2.3 Measurements of the Group Delay

Measurements at several QD-VCSEL injection current are studied. The amplified spontaneous emission (ASE) center frequency below threshold and the lasing frequency of the QD-VCSEL above threshold are recorded first on the spectrum analyzer.

Signal group delay increases when we increase the injection current. Group delay of the 10-GHz sinusoidal signal for various injection currents are shown in Fig. 3.5.

For a 10-GHz sinusoid, the maximum group delay of 41 ps at 1 mA is observed. When injection current is 1mA, delay of sinusoidal signals for 5, 6, 7, 8, 9, and 10-GHz are plotted in Fig. 3.6.

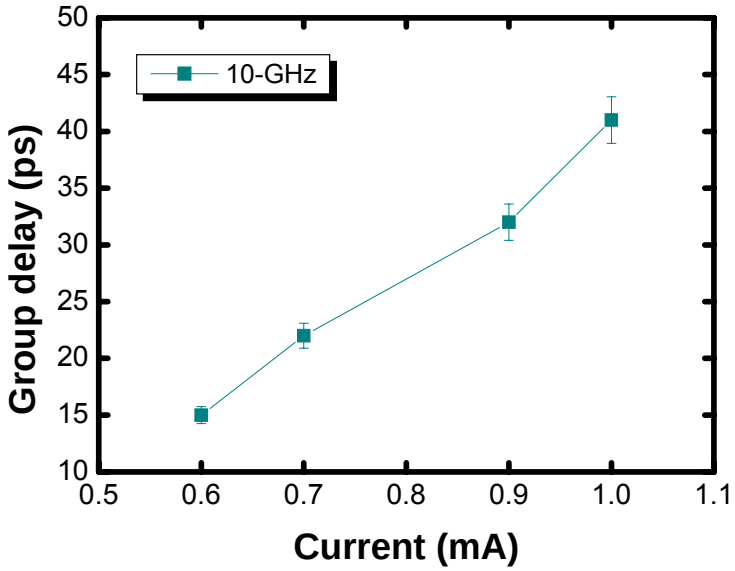

Figure 3.5. Group delay of the 10-GHz sinusoidal signal for injection current I=0.6, 0.7, 0.9, and 1 mA [12].

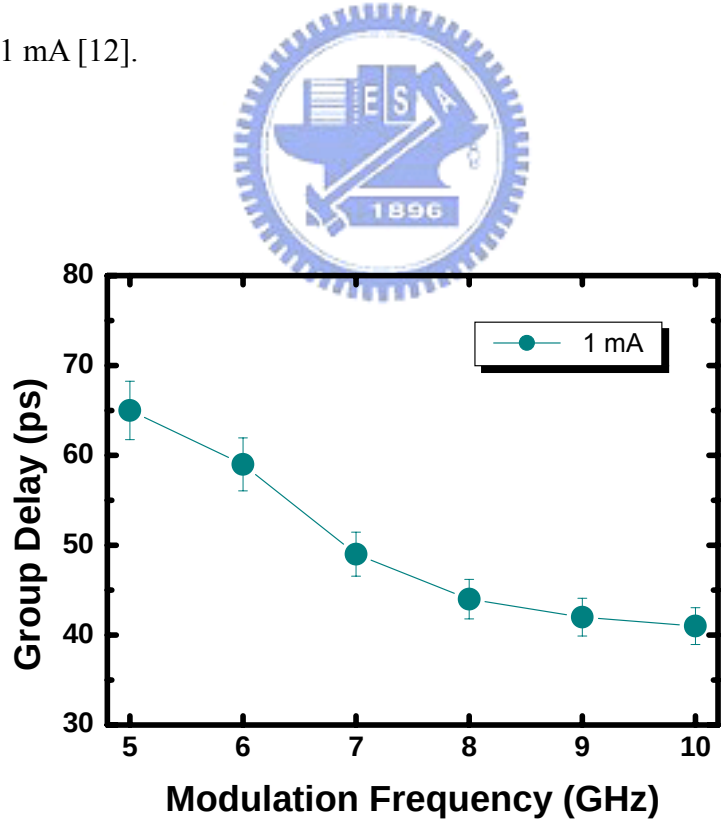

Figure 3.6. Group delay of sinusoidal signals for 5, 6, 7, 8, 9, and 10 GHz at 1 mA [12].

3.3 THEORETICAL ANALYSIS AND SIMULATION

3.3.1 Introduction

Slow-light using quantum-well Fabry-Perot laser [10], quantum-well VCSEL [11], and the quantum-dot VCSEL [12] have been experimentally demonstrated. In [12], the tunable delay of sinusoidally modulated light signal up to 10 GHz is achieved. However, clear physical mechanism and explanation why there is such a high-bandwidth delay in vertical-cavity laser, is rarely provided. On the other hand, delay of 1 GHz sinusoidally modulated signal in a vertical-cavity semiconductor optical amplifier (VCSOA) is studied [36], and a Fabry-Perot model is used to explain the experiment result. Since the filter phase response changes very fast in the vicinity of the cavity resonance frequency, the group delay theory in [36] is suitable only for use in the low modulated frequency (<1 GHz) signal, rather than the possible several GHz range bandwidth use of the semiconductor slow-light optoelectronic devices. Chuang et al [31, 32] used transfer matrix formalism to analyze delay of signal of several GHz in a semiconductor active waveguide, and can reshape square waves of 5-GHz bandwidth. In this study, we adopt the approach similar to [31, 32] to analyze slow-light in active vertical-cavity optoelectronic devices.

3.3.2 Explanation and Simulation

The experimental results with stress on the group delay, injection current, and modulation frequency can be explained by use of VCSEL amplifier model [37].

Schematic optical spectrum of the reflection from a VCSEL used to explain the group delay is shown in Fig. 3.7. The input signal power in the experiment is -14 dBm or 40 μW , which is much larger than the laser emission power of 8.5 μW of the QD VCSEL biased at 1 mA. The strong input light increases the photon number inside the laser cavity, and then expedites stimulated emission rate of the laser medium, thus depleting the carrier density to a level that is below its lasing threshold [37]. Therefore the VCSEL acts like an amplifier at this time [37]. To explain why group delay increases with the injection current and its trend as a function of modulation frequency, the VCSEL amplifier model is used to carry out some simulations using equivalent Fabry-Perot etalon method [15]. The VCSEL amplifier model used to carry out theoretical simulations is depicted in Fig. 3.8.

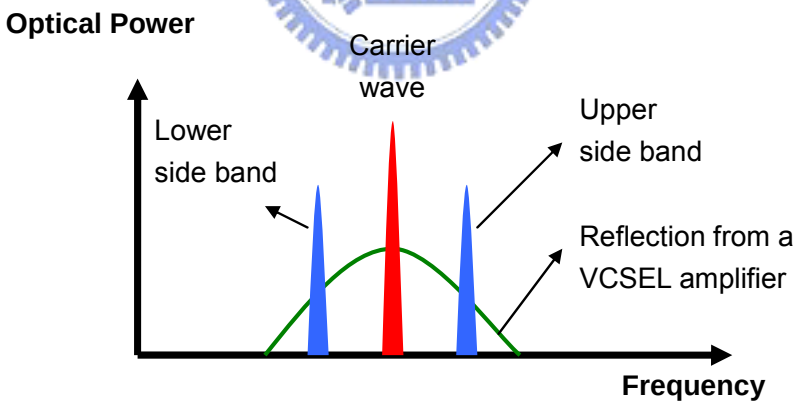

Figure 3.7. Schematic optical spectrum of the reflection from a VCSEL used to explain the group delay.

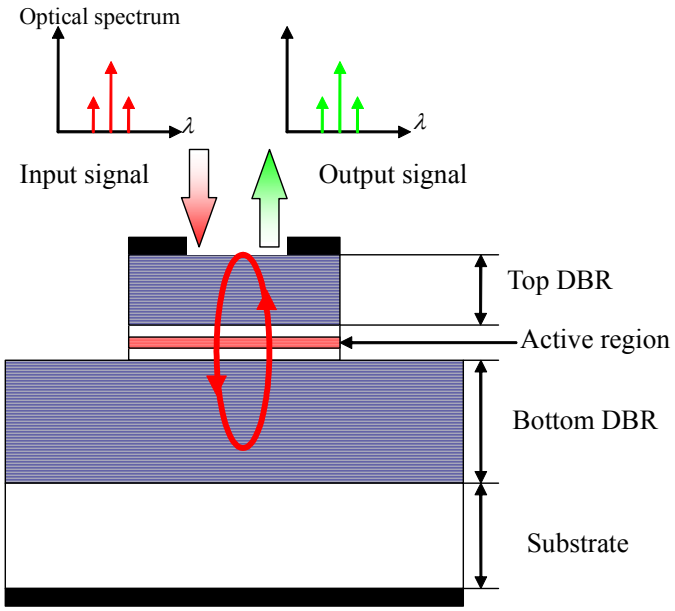

Figure 3.8. VCSEL amplifier model used to carry out theoretical simulations.

The maximum achievable reflectivity of top and bottom DBRs is about 99.65% and 99.66% respectively [16], due to a relatively high doping ($N_a, N_d = 2 \sim 3 \times 10^{18}$ cm^{-3}) and then considerable absorption optical losses. An input light signal is incident on an active VCSEL resonator below its lasing threshold. The filter phase and the intensity response are the quantities of interests. Because phase shift of the distributed Bragg mirror is zero at the Bragg frequency and a slowly-changing linear function in the vicinity of Bragg frequency [1], the mirror phase shift can be neglected. The thickness of the center region Lc is 3 λ, where λ is the laser wavelength in the cavity. The top and bottom DBR penetration depths are calculated and are 1.5 λ respectively. The effective cavity length Lc_{eff} is thus 6 λ in the QD VCSEL. The internal loss in the device of $10\,\text{cm}^{-1}$ is assumed in the simulations. The reflection

coefficient of the asymmetric Fabry-Perot etalon is [3]:

$$r = \frac{r_1 + r_2 \cdot e^{-i\,2\,kL_{ceff}}}{1 - r_1 \cdot r_2 \cdot e^{-i\,2\,kL_{ceff}}} \tag{3.8}$$

where r_1 and r_2 are the real reflection coefficient of the effective top and bottom mirror respectively, $k = 2\pi\nu n_e / c + i(g - \alpha_i)/2$ is the complex propagation constant, where c is the light speed in the air, n_e is the effective index of the graded-index separate confinement heterostructure (GRINSCH) active region, g is the modal gain, and α_i is the intrinsic internal loss. The reflection intensity response and the phase shift of the resonator are $|r(\nu)|^2$ and $\phi(\nu) = Arg[r]]$, respectively

Fig. 3.9 and Fig. 3.10 show the simulated intensity response and the corresponding phase response of the VCSEL amplifier for three different modal gain values. When $g = 0.7\,g_{th}$, the amplitude response is flat, behaving as an all-pass filter [10]. Note that phase response changes slowly when $0.7\,g_{th}$ increases to $0.8\,g_{th}$, and then becomes steeper swiftly when modal gain is close to threshold.

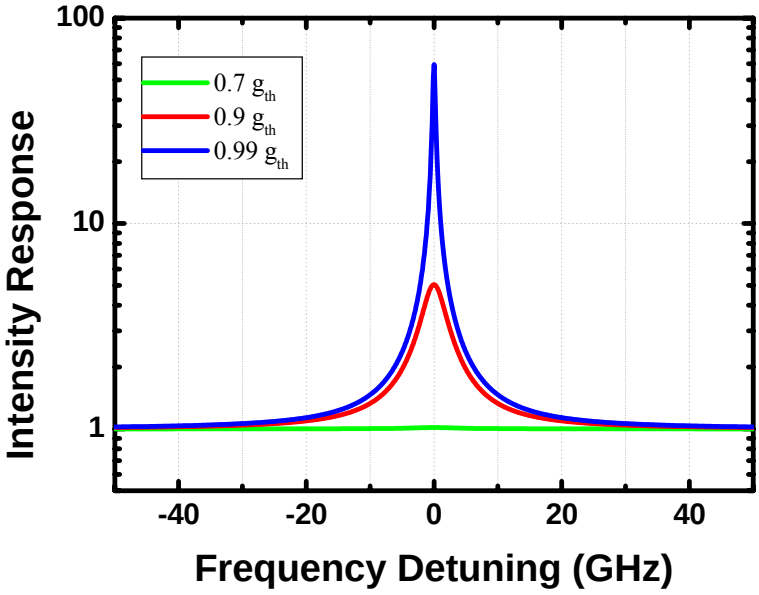

Figure 3.9. Simulated amplitude response of the VCSEL amplifier for three different modal gain values of $0.7\ g_{th}$, $0.9\ g_{th}$, and $0.99\ g_{th}$.

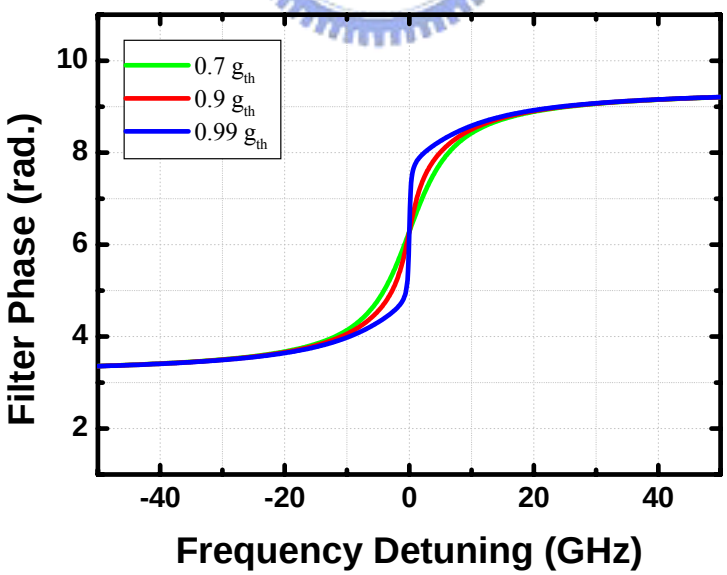

Figure 3.10. Corresponding simulated phase response of the VCSEL amplifier for the same three different modal gain values.

The group delay of an optical sinusoidal signal, given by $\tau_{fm} = [\phi(\nu_0 + f_m) - \phi(\nu_0 - f_m)]/(4\pi f_m)$, can be deduced from the slope of the phase response [32], where f_m is sinusoidal modulation frequency of the input light signal. The proof of the formula is in the appendix. Simulated delay as a function of modulation frequency between 1 and 10 GHz for different modal gains is plotted in Fig. 3.11. To have a comparison between simulation results and experimental results, experimental results for injection current 1 mA is also shown in Fig. 3.11. Fig. 3.12 shows the simulated delay as a function of modal gain for different modulation frequencies.

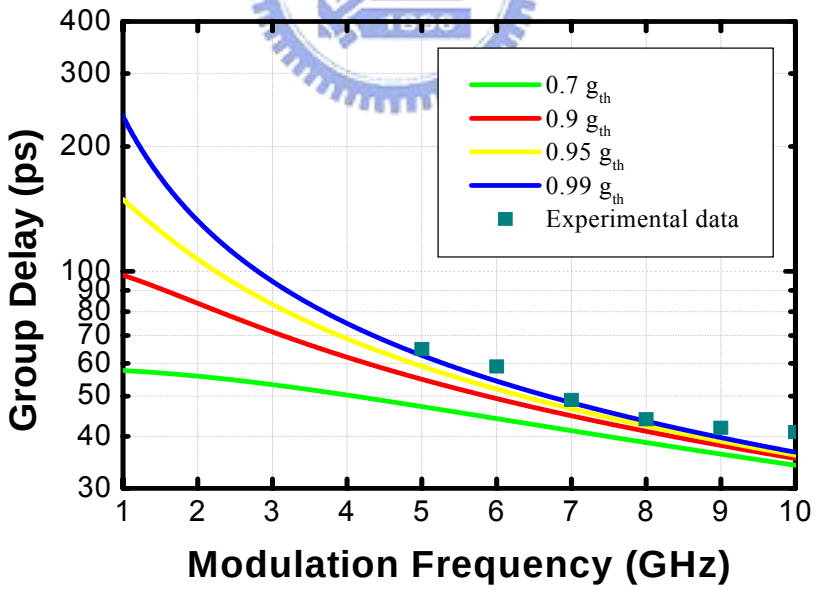

Figure 3.11. Simulated group delay as a function of modulation frequency for different modal gains. Experimental data is also shown in this figure

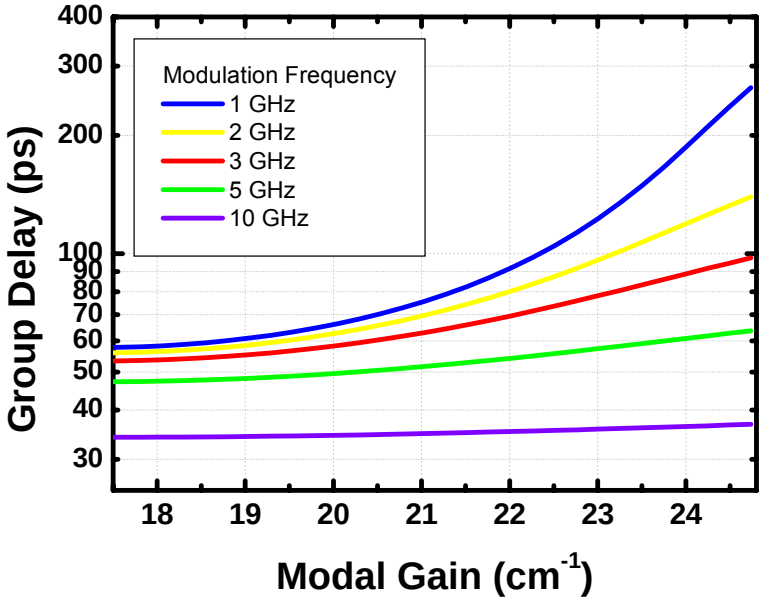

Figure 3.12. Simulated group delay as a function of modal gain for different modulation frequencies

The simulation results agree well with the experimental results. The group delay decreases with the increased modulation frequency. This is because phase response changes fast in the vicinity of etalon resonance frequency (phase slope is large), and phase slope is small when the modulation frequency is large. On the other hand, group delay increases with the increased modal gain, because the phase response becomes steeper. Note that the calculated delay of the single-tone 1-GHz signal can be high up to 240 ps, corresponding to a delay-bandwidth product (DBP) [8] of 0.24. Larger simulated DBP of 0.37 can be for the single-tone 10-GHz signal, which is slightly smaller than the experimental value of 0.41.

If the -14 dBm strong input light signal makes the slave laser below its lasing threshold, spectrum hole burning effect will appear, making index and gain coefficient dependent on wavelength. Our simulation does not take this wavelength-dependent gain into consideration as in [38]. Moreover, because gain value and refraction index of the laser medium are coupled to each other through famous Kramer-Kronig relation, this decrease in gain value can shifts the cavity resonance frequency to a longer wavelength (red-shift).[2, 40]. It can be shown that the amount of this red-shift frequency change is directly proportional to the linewidth enhancement factor of the laser gain medium [40, 41]:

$$\Delta f = \frac{\alpha_e}{2} v_g \cdot (g_s - g_0) \tag{3.9}$$

where α_e is the linewidth enhancement factor or α-parameter, v_g is the group velocity of light in the laser cavity, g_s is the suppressed modal gain of the VCSEL, and g_0 is the small-signal modal gain of the VCSEL. It has been predicted that quantum-dot (QD) lasers, in principle, should exhibit a near-zero α-parameter, due to the discrete density of states and symmetric gain spectrum [18]. Our simulation assumes that the carrier frequency is exactly in the VCSEL cavity mode, and should be in best agreement with the experiment when the input signal power is not large enough to change the resonance frequency.

On the other hand, we think that four wave mixing (FWM) effect is not obvious in the experiment. Because the large DBR mirror reflectivity, the short cavity length in the VCSEL and the fact that the carrier wave and the signal sidebands cannot be in the

VCSEL cavity mode concurrently, the superposition of the multiple reflected waves can be destructive interference if it is not in the cavity mode. Consequently, nonlinear coherent interaction between light of different wavelength such as FWM or coherent population oscillation (CPO) can be negligible in the study.

The simulation shown here is done assuming the carrier frequency is in the cavity mode exactly and strong input light signal causes the slave laser below its lasing threshold. Red-shift resonance and the influence of the spectrum hole burning effect need to be included to fully realize the physical mechanism. These are beyond the scope of this master degree thesis and complete investigation is underway.

3.4 SUMMARY

In this chapter, slowing light using vertical-cavity surface-emitting lasers (VCSELs) is explained and simulated using VCSEL amplifier model. Simulated results and result are qualitatively in a good agreement. With the aid of the filter phase analysis, the simulation explains that group delay increases with increased modal gain. Besides, the simulations predict the slow-light capability of delaying single-tone sinusoidal signal of 1 to 5 GHz. Further, the principle should not be suitable for use in VCSELs only. It can be generalized to the general kinds of semiconductor lasers.

Chapter 4

SLOWING LIGHT USING INJECTION-LOCKING OF VCSELS

4.1 INTRODUCTION

In this chapter, we will study RF delay or optical delay in a semiconductor laser far above its lasing threshold. This is a standard laser injection-locking problem. Before any experimental study is described, it is worthwhile reviewing the basic theory of the injection-locking of the semiconductor lasers first.

4.2 INTRODUCTION TO INJECTION-LOCKING OF SEMICONDUCTOR LASERS – RATE EQUATIONS AND STEADY-STATE ANALYSIS [39-42]

When an external laser light (master laser) enter into the resonator of a following laser (slave laser), the behavior of the photon and the carrier in the semiconductor lasers can be described by use of the rate equation formalism below:

$$photon: \quad \frac{d}{dt}\mathrm{E}_{\mathrm{SL}} = \{j\omega + \frac{1}{2}[g \cdot v_g - \frac{1}{\tau_p}]\} \cdot \mathrm{E}_{\mathrm{SL}}(t) + \eta \cdot f_d \cdot E_{ML}(t) \tag{4-1}$$

$$carrier: \quad \frac{d}{dt}N = J - \frac{N(t)}{\tau_{sp}} - g \cdot v_g \cdot E_0(t)^2 \tag{4-2}$$

In these equations, E_{SL}, E_{ML}, and N are the slave laser electric field, the master laser electric field, and the carrier density in the slave laser's active region, respectively. g is the differential gain. τ_p and τ_{sp} are the photon and carrier lifetimes, respectively. Fd is the longitudinal mode spacing, and η is the coupling coefficient.

To solve these united differential equations, we can set:

$$\mathrm{E}_{SL}(t) = E_0(t) \cdot e^{i(\omega_0 t + \phi_0(t))} \tag{4-3}$$

$$\eta \cdot E_{ML}(t) = E_1 \cdot e^{i(\omega_1 t)} \tag{4-4}$$

After substitution into the rate equation, we can get

$$\omega - \omega_0 = \frac{1}{2} \cdot \alpha \cdot v_g \cdot (g_s - g_{th}) \tag{4-5}$$

where α is the linewidth enhancement factor (α-parameter). Because gain coefficient and refraction index of the gain materials are coupled to each other, changing in gain can lead to shift of the cavity resonance.

Using (4-3) ~ (4-5), the photon rate equation can then be converted to the amplitude-phase format

$$\frac{d}{dt}E_0(t) = \frac{1}{2}v_g g(N - N_{th}) \cdot E_0(t) + f_d \cdot E_1 \cdot \cos[\Delta\omega \cdot t - \phi_0(t)] \tag{4-6}$$

$$\frac{d}{dt}\phi_0(t) = \frac{1}{2}v_g g(N - N_{th}) + f_d \cdot \frac{E_1}{E_0(t)}\sin[\Delta\omega \cdot t - \phi_0(t)] \tag{4-7}$$

where $\Delta\omega = \omega_1 - \omega_0$ is the angular frequency detuning between the free-running lasers. After some algebra derivations, and assuming the steady locking state, the

depleted carrier density can be shown

$$\Delta\widetilde{\mathrm{N}}_{\mathrm{i}} = -2\frac{f_d}{v_g \cdot g}\cdot\frac{E_1}{\widetilde{E}_0}\cdot\cos(\phi_L) \tag{4-8}$$

where ϕ_L is the phase of the slave laser with respect to the master laser, and $\widetilde{\mathrm{E}}_0$ is the constant slave laser electric field amplitude. The light intensity within the resonator can easily be shown

$$(\widetilde{E}_0)^2 = \frac{(\widetilde{\mathrm{E}}_{0\mathrm{s}})^2 - \frac{\tau_p}{\tau_s}\cdot\Delta\widetilde{N}_i}{1+\tau_s\cdot\tau_p\cdot\Delta\widetilde{N}_i} \tag{4-9}$$

The stable locking range, where the slave laser and the master laser operate in the same wavelength, can be shown [1985 JQE Henry & Dutta]

$$-f_d\cdot\frac{E_1}{\widetilde{E}_0}\sqrt{1+\alpha^2} < \omega_1 - \omega_0 < f_d\cdot\frac{E_1}{\widetilde{E}_0} \tag{4-10}$$

From this equation, the stable locking range is wide when the intensity of the master laser is much larger than the slave laser. Besides, the appearance of the α-parameter make the stable locking range not symmetric with respect to the free-running slave laser frequency. Outside the stable locking range, complex nonlinear phenomena such as chaos, four wave mixing, and nonlinear dynamics etc will appear, which are above the scope of this thesis.

4.3 EXPERIMENTAL SETUP

In this study we explore a slow light scheme using an injection-locked semiconductor laser. We demonstrate that the RF delay or optical delay can largely increase due to

the amplified signal sideband.

Fig. 4.1 shows the experimental setup. The 1.3-μm tunable laser diode produces the continuous-wave (CW) probe light. A sinusoidal light signal is then generated after the CW probe light is sent through a Mach-Zehnder interferometric waveguide electro-optical modulator, which is driven by a vector network analyzer (HP 8270ES). variable optical attenuator is used to control the power of the light signal, which is fixed to -14 dBm (~40 μW) in this study. A polarization controller (PC) is used to adjust the polarization of the input light signal. The input light signal enters the slave semiconductor laser through an optical circulator (OC). A small part of the output light signal enter an optical spectrum analyzer (OSA), and the greater part of the output light signal goes into the photodetector and transforms into electrical RF signal. The RF signal is amplified by a RF amplifier and then goes into the network analyzer. The RF amplitude frequency response and phase frequency response of the output signal are directly observed by measuring the amplitude and the phase response of the S21 port of the network analyzer, calibrated with the responses when the input light signal is away from the free-running slave semiconductor laser wavelength. Amplitude response and phase response are measured at various wavelength detuning values ($\Delta\lambda = \lambda_{carrier\ wave\ of\ input} - \lambda_{free\text{-}running\ slave}$).

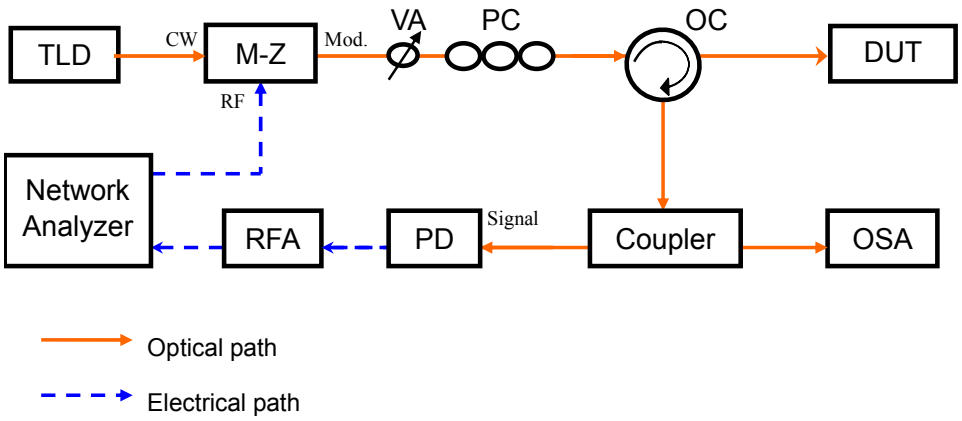

Figure 4.1. Experimental setup used for RF delay or optical delay measurement. (TLD: tunable laser diode; VA: variable attenuator; PC: polarization controller; OC: optical circulator; OSA: optical spectrum analyzer; PD: photodetector; RFA: RF amplifier; DUT: device under test, which is the quantum-dot VCSEL in this study).

The slave semiconductor laser used in this study is a monolithically single-mode quantum-dot (QD) vertical-cavity surface-emitting laser (VCSEL) [35]. Fig. 4.2 shows the light-current curve of the slave quantum-dot VCSEL used in this study. In the study, the injection current of the slave VCSEL is 1.7 mA, which is well above its lasing threshold.

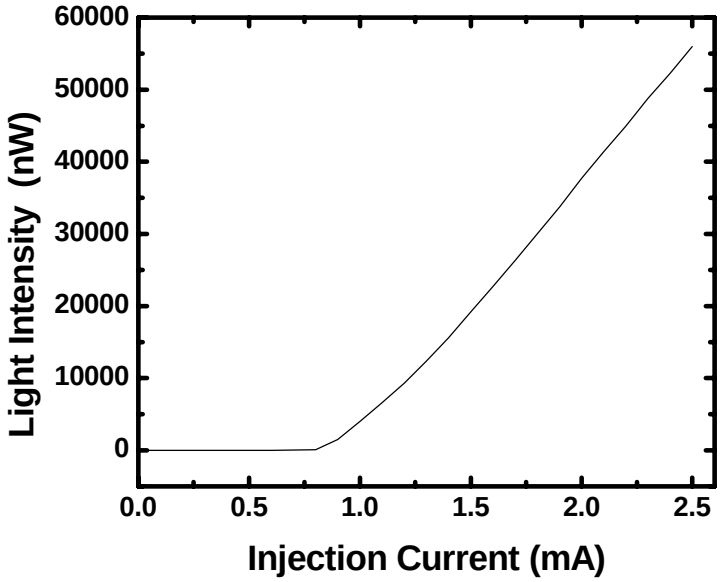

Figure 4.2. Light-current curve of the quantum-dot VCSEL used in this study. The threshold current is about 0.8 mA.

4.4 EXPERIMENTAL RESULTS AND DISCUSSION

Fig. 4.3 and Fig. 4.4 show the relative amplitude response and the RF phase change response for various wavelength detuning values. Increasing wavelength detuning shifts the amplitude and phase response to higher RF frequency. RF phase change of nearly 2π can be achieved if the modulation frequency is high enough. It is observed that the dip in the amplitude response also accompanies a RF phase change about 200 degree.

Fig. 4.5 shows the optical spectrum at wavelength detuning of 0.1122nm, and the modulation frequency is 14 GHz, corresponding to a RF phase change of 200 degree.

Fig. 4.6 shows the optical spectrum at wavelength detuning of 0.1386nm.

Modulation frequency is 19 GHz, corresponding to RF phase change of 250 degree for the wavelength detuning.

According to the optical spectra, the upper sideband of the signal is amplified and is 10 dB larger than the lower sideband. Moreover, the slave VCSEL is mot in the stable locking regime, provided the slave laser and the master laser do not operate in the same lasing wavelength. Thus, the upper sideband is amplified because of the complex nonlinear dynamic phenomena and the slave VCSEL acts as a regenerative amplifier.

Compared with the VCSEL amplifier below its lasing threshold in chapter 3, although slow-light based on the injection-locking mechanism can have more optical delay, the amplified sideband may induce signal distortion (appendix) , which is not wanted for optical delay line use. Besides, the complexity of nonlinear dynamics largely increases difficulty in designing slow-light devices.

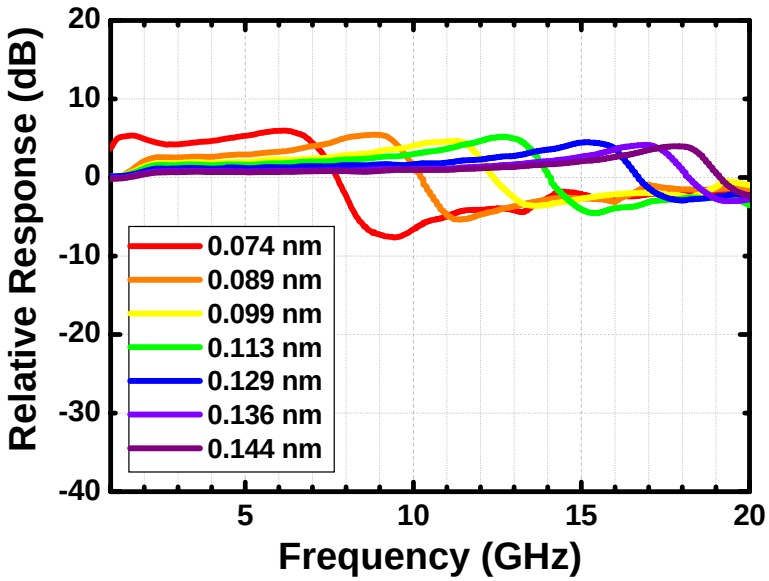

Figure 4.3. Measured relative amplitude response of an injection-locked VCSEL for various wavelength detuning values. The input signal power before entering the VCSEL is -14 dBm throughout the study.

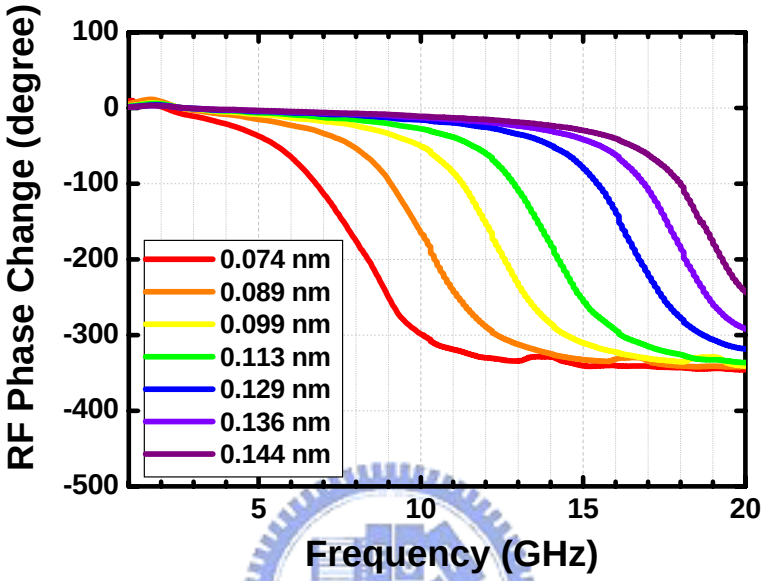

Figure 4.4. Measured corresponding RF phase change response of an injection-locked VCSEL for various wavelength detuning values.

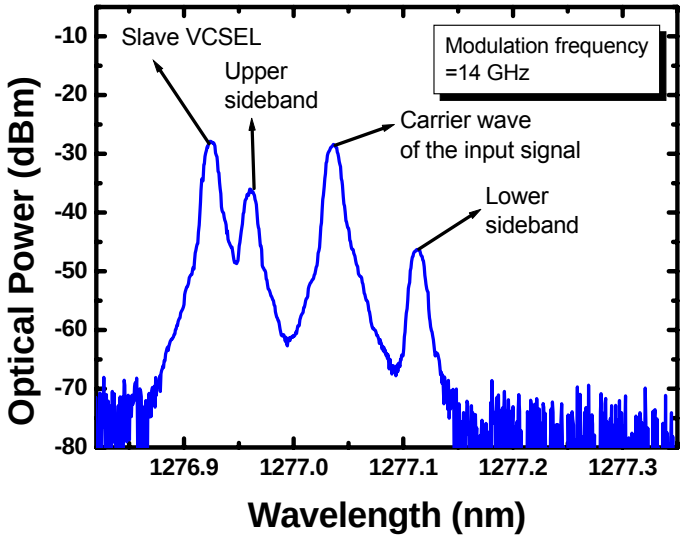

Figure 4.5. Optical spectrum at wavelength detuning of 0.1122nm. Modulation frequency is 14 GHz, corresponding to RF phase change of 200 degree for the wavelength detuning.

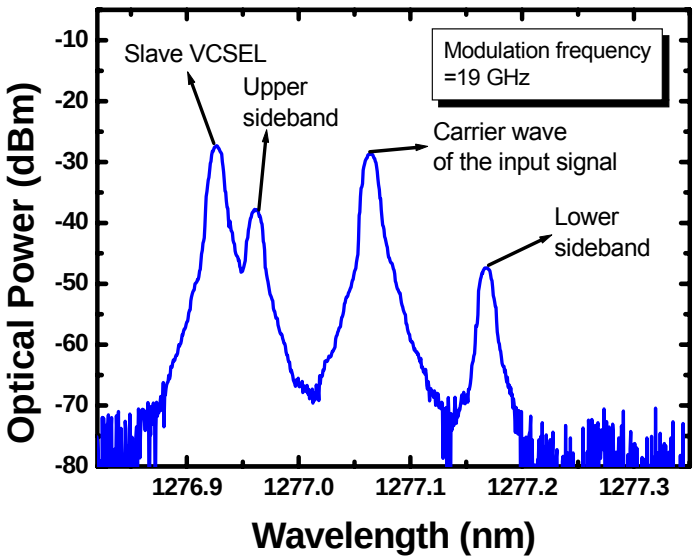

Figure 4.6. Optical spectrum at wavelength detuning of 0.1386nm. Modulation

frequency is 14 GHz, corresponding to RF phase change of 250 degree for the wavelength detuning.

4.5 SUMMARY

The chapter concludes the study of achieving RF delay or optical delay using injection-locking of the VCSEL. The amplitude response and phase response shift with increased wavelength detuning. The optical spectrum is studied, which reflects the slave laser does not operate in the stable locking regime.

Chapter 5

CONCLUSION

In this thesis, slowing light using vertical-cavity surface-emitting lasers (VCSELs) is explained and simulated using VCSEL amplifier model. Simulated results and result are qualitatively in a good agreement. With the aid of the filter phase analysis, the simulation explains that group delay increases with increased modal gain and decreases with increased modulation frequency. Besides, the simulations predict the VCSEL's capability of delaying single-tone sinusoidal signal of 1 to 5 GHz.

Moreover, understanding the basic principle behind allow us to design optimized optical delay line using VCSEL amplifier scheme. Further, the principle should not be suitable for use in VCSELs only. It can be generalized to the general kinds of semiconductor lasers.

RF delay or optical delay using injection-locking of VCSELs is studied in the thesis. Optical spectra show that the VCSEL is not in the stable-locking range. The VCSEL acts as a regenerative amplifier, making one of the signal side band much larger than the other. From the description in the appendix of this thesis, a reflected signal with one of its side band amplified can cause signal distortion.

In summary, this thesis explores the novel use of semiconductor lasers as optical delay line and gives at least qualitative explanation. The functionality, compactness, and practicality nature will make semiconductor lasers promising candidates for the novel generation of optical delay lines in high-speed optical network in the future.

BIBLIOGRAPHY

[1] A. Yariv and P. Yeh, *Photonics*, 7th ed., Oxford University Press, 2007.

[2] A. Yariv, *Quantum Electronics*, 3d ed., Wiley, 1989.

[3] S. L. Chuang, *Physics of Optoelectronic Devices,* Wiley-Interscience, 1995.

[4] Zh. I. Alferov, "Double Heterostructure Lasers: Early Days and Future Perspectives," *IEEE J. Sel. Top. Quantum Electron*. 6, 832-840, 2000.

[5] N. N. Ledentsov, M. Grundmann, F. Heinrichsdorff, D. Bimberg, V. M. Ustinov, A. E. Zhukov, M. V. Maximov, Zh. I. Alferov, and J. A. Lott, "Quantum-Dot Heterostructure Lasers," *IEEE J. Sel. Top. Quantum Electron*. 6, 439-451, 2000.

[6] M. Sugawara, N. Hatori, M. Ishida, H. Ebe, Y Arakawa, T. Akiyama, K. Otsubo, T. Yamamoto, and Y. Nakata, "Recent progress in self-assembled quantum-dot optical devices for optical telecommunication: temperature-insensitive 10Gbs^{-1} directly modulated lasers and 40Gbs^{-1} signal-regenerative amplifiers," *J. Phys. D: Appl. Phys.* 38, 2126–2134, 2005.

[7] D. Bimberg, "Quantum dots for lasers, amplifiers and computing," *J. Phys. D: Appl. Phys.* 38, 2055–2058, 2005.

[8] C. J. Chang-Hasnain and S. L. Chuang, "Slow and Fast Light in Semiconductor Quantum-Well and Quantum-Dot Devices," *J. Lightwave Technol.* 24, 4642-4654, 2006.

[9] P. C. Ku, C. J. Chang-Hasnain, and S L Chuang, "Slow light in semiconductor heterostructures," , *J. Phys. D: Appl. Phys*. 40, R93–R107, 2007.

[10] S. Minin, M. Fisher, and S. L. Chuang, “Current-controlled group delay using a semiconductor Fabry–Pérot amplifier,” *Appl. Phys. Lett.*, vol. 84, no. 17, pp. 3238–3240, 2004.

[11] X. Zhao, P. Palinginis, B. Pesala, C. J. Chang-Hasnain, and P. Hemmer, “Tunable ultraslow light in vertical-cavity surface emitting laser amplifier,” *Opt. Express*, vol. 13, no. 20, p. 7899, 2005.

[12] P. C. Peng, C. T. Lin, H. C. Kuo, W. K. Tsai, J. N. Liu, S. Chi, S. C. Wang, G. Lin, H. P. Yang, K. F. Lin, and J. Y. Chi, “Tunable slow light device using quantum dot semiconductor laser”, *Optics Express*, Vol. 14, Issue 26, pp. 12880-12886 , 2006.

[13] E. O. Kane, “The k.p method,” Chapter 3, in R. K. Willardson and A. C. Beer, Eds., *Semiconductors and Semimetals*, Vol.1, Academic, 1966.

[14] J. Singh, *Electronic and Optoelectronic Properties of Semiconductor Structures*, Cambridge University Press, 2003.

[15] L. A. Coldren and S. W. Corzine, *Diode Lasers and Photonic Integrated Circuits*, Wiley-Interscience, 1995.

[16] V. M. Ustinov, A. E. Zhukov, A. Y. Egorov, and N. A. Maleev, *Quantum Dot Lasers*, Oxford University Press, 2003.

[17] J. Singh, *Semiconductor Optoelectronics – Physics and Technology*, McGraw-Hill, Inc., 1995.

[18] Z. Mi and P. Bhattacharya, "Analysis of the Linewidth-Enhancement Factor of Long-Wavelength Tunnel-Injection Quantum-Dot Lasers," *J. Quantum Electron.* 43, 363-369, 2007.

[19] Joe T. Mok and Benjamin J. Eggleton, “Expect more delays”, *Nature*, Vol 433, 24 Feb 2005

[20] G. Lenz, B. J. Eggleton, C. K. Madsen, and R. E. Slusher, “Optical delay lines based on optical filters”, *IEEE J. Quantum Electronics*, Vol. 37, NO. 4, April

2001.

[21] C. J. Chang-Hasnain, P.-C. Ku, J. Kim, and S. L. Chuang, "Variable optical buffer using slow light in semiconductor nanostructures," *Proc. IEEE*, vol. 9, no. 11, p. 1884, Nov. 2003.

[22] L. V. Hau, S. E. Harris, Z. Dutton, and C. H. Behroozi, "Light speed reduction to 17 meters per second in an ultra cold atomic gas", *Nature*, Vol. 397, Feb 1999.

[23] J. E. Field, K. H. Hahn and S. E. Harris, "Observation of electromagnetically induced transparency in collisionally broadened lead vapor," *Phys. Rev. Lett.* 67 3062, 1991.

[24] M. S. Bigelow, N. N. Lepeshkin, and R. W. Boyd, "Observation of ultraslow light propagation in a ruby crystal at room temperature," *Phys. Rev. Lett.*, vol. 90, no. 11, p. 113 903, Mar. 2003.

[25] P.-C. Ku, F. Sedgwick, C. J. Chang-Hasnain, P. Palinginis, T. Li, H.Wang, S.-W. Chang, and S. L. Chuang, "Slow light in semiconductor quantum wells," *Opt. Lett.,* vol. 29, no. 19, pp. 2291–2293, Oct. 2004.

[26] P. Palinginis, F. Sedgwick, S. Crankshaw, M. Moewe, and C. J. Chang-Hasnain, "Room temperature slow light in a quantum-well waveguide via coherent population oscillation," *Opt. Express,* vol. 13, no. 24, pp. 9909–9915, Nov. 2005.

[27] H. Su and S. L. Chuang, "Variable optical delay using population oscillation and four-wave-mixing in semiconductor optical amplifiers," *Opt. Express*, vol. 14, no. 11, pp. 4800–4807, May 2006.

[28] H. Su and S. L. Chuang, "Room temperature slow light with semiconductor quantum-dot devices," *Opt. Lett.*, vol. 31, no. 2, pp. 271–273, Jan. 2006.

[29] H. Su and S. L. Chuang, "Room temperature slow and fast light in quantum dot semiconductor optical amplifiers," *Appl. Phys. Lett*., vol. 88, no. 6, pp. 061102-1–061102-3, Feb. 2006.

[30] J. K. S. Poon, L. Zhu, G. Y. DeRose, and A. Yariv, “Transmission and group delay of microring coupled-resonator optical waveguides”, *Opt. Lett.* 31, 456-458, 2006.

[31] M. R. Fisher, S. Minin, and S. L. Chuang, “Tunable optical group delay in an active waveguide semiconductor resonator,” IEEE J. Sel. Topics Quantum Electron., vol. 11, no. 1, pp. 197–203, Jan./Feb. 2005.

[32] M. R. Fisher, and S. L. Chuang, “Variable Group Delay and Pulse Reshaping of High Bandwidth Optical Signals”, *IEEE J. Quantum Electron.* 41, 885-891, 2005.

[33] H. Altuga and J. Vuckovic, “Two-dimensional coupled photonic crystal resonator arrays”, *Appl. Phys. Lett.*, Vol.84, 161-163, 2004.

[34] J. K. S. Poon, J. Scheuer, Y Xu, and A. Yariv, “Designing coupled-resonator optical waveguide delay lines”, *J. Opt. Soc. Am. B* 21, 1665-1673, 2004.

[35] Y. H. Chang, P. C. Peng, W. K. Tsai, G. Lin, F. I. Lai, R. S. Hsiao, H. P. Yang, H. C. Yu, K. F. Lin, J. Y. Chi, S. C. Wang, and H. C. Kuo, “Single-mode monolithic quantum-dot VCSEL in 1.3 um with sidemode suppression ratio over 30 dB,” *IEEE Photon. Tech. Lett*. 18, 847-849, 2006.

[36] N. Laurand, S. Calvez and M. D. Dawson, and A. E. Kelly, "Slow-light in a vertical-cavity semiconductor optical amplifier," *Opt. Express* 14, 6858-6863, 2006.

[37] X. Zhao, Y. Zhou, C. J. Chang-Hasnain, W. Hofmann, and M. C. Amann, “Novel modulated-master injection-locked 1.55-μm VCSELS,” *Opt. Express* 14, 10500-10507, 2006.

[38] M. R. Fisher and S. L. Chuang, “Asymmetric nonlinear transmission spectra of Fabry-Perot laser amplifiers,” *IEEE Photon. Tech. Lett.* 18, 409-411, 2006.

[39] A. Murakami, K. Kawashima, and K. Atsuki, ”Cavity Resonance Shift and Bandwidth Enhancement in Semiconductor Lasers With Strong Light Injection,” *IEEE J. Quantum Electron.* QE-39, pp. 1196-1204, 2003.

[40] F. Mogensen, H. Olesen, and G. Jacobsen, "Locking Conditions and Stability Properties for a Semiconductor Laser with External Light Injection," *IEEE J. Quantum Electron*. QE-21, 784-793, 1985.

[41] R. Lang, "Injection Locking Properties of a Semiconductor Laser," *IEEE J. Quantum Electron.* QE-18, 976-983, 1982.

[42] C. H. Henry, N. A. Olsson, and N. K. Dutta, "Locking Range and Stability of Injection Locked 1.54 pm InGaAsP Semiconductor Lasers," *IEEE J. Quantum Electron.* QE-21, 1152-1156, 1985.

[43] X. Zhao, Y. Zhou, C. J. Chang-Hasnain, W. Hofmann, and M. C. Amann, "Slow and fast light using master-modulate injection-locked VCSELs," *Conf. on Lasers and Electro-Optics/Quantum Electronics and Laser Science (CLEO/QELS, Long Beach, CA, USA) (Piscataway, NJ: IEEE)*, 2006.

Appendix

REFLECTION OF A SINGLE-TONE OPTICAL SIGNAL FROM A PHOTONIC DEVICE OR A SYSTEM [1, 2, 31, 32]

Let us consider the reflection of an optical sinusoidal signal from a photonic device. The sinusoidal signal is produced through amplitude modulation (AM), so input complex electric field of light can be written as the carrier wave plus two sidebands:

$$E_{in}(t) = A_0 \cdot e^{i2\pi\nu_0 t} \cdot (1 + A_1 \cdot e^{i2\pi \cdot f_m \cdot t} + A_1 \cdot e^{-i2\pi \cdot f_m \cdot t}) \tag{A.1}$$

where f_m is modulation frequency of the sinusoidal, and ν_0 is the carrier wave frequency, A_0 and A_1 are the Fourier spectrum of the light signal. The optical signal reflecting from an optical device or a system can be written

$$\begin{aligned} E_{reflect}(t) = {} & A_0 \cdot \sqrt{R(\nu_0)} \cdot e^{i2\pi\cdot\nu_0 t} \cdot e^{-i\phi(\nu_0)} + A_1 \cdot e^{i2\pi\cdot(\nu_0+f_m)\cdot t} \cdot \sqrt{R(\nu_0+f_m)} \cdot e^{-i\phi(\nu_0+f_m)} \\ & + A_1 \cdot e^{i2\pi\cdot(\nu_0-f_m)\cdot t} \cdot \sqrt{R(\nu_0-f_m)} \cdot e^{-i\phi(\nu_0-f_m)} \end{aligned} \tag{A.2}$$

where R is the reflectivity of the optical device, which is a function of light frequency. We now consider the situation where $R(\nu_0 + f_m) \cong R(\nu_0 - f_m)$. In this case, the reflected signal can be rewritten

$$
\begin{aligned}
E_{reflect}(t) &= B_0 \cdot e^{i2\pi \cdot \nu_0 t} \cdot e^{i\phi(\nu_0)} \cdot [1 + B_1 \cdot e^{i2\pi \cdot f_m \cdot t} \cdot e^{-i[\phi(\nu_0 + f_m) - \phi(\nu_0)]} + B_1 \cdot e^{-i2\pi \cdot f_m \cdot t} \cdot e^{-i[\phi(\nu_0 - f_m) - \phi(\nu_0)]}] \\
&= B_0 \cdot e^{i2\pi \cdot \nu_0 t} \cdot e^{i\phi(\nu_0)} \cdot [1 + B_1 \cdot e^{i2\pi \cdot f_m \cdot t} \cdot e^{-i\frac{[\phi(\nu_0 + f_m) - \phi(\nu_0)]}{f_m} f_m} + B_1 \cdot e^{-i2\pi \cdot f_m \cdot t} \cdot e^{-\frac{i[\phi(\nu_0 - f_m) - \phi(\nu_0)]}{f_m} f_m}]. \\
&\cong B_0 \cdot e^{i2\pi \cdot \nu_0 t} \cdot e^{i\phi(\nu_0)} \cdot [1 + B_1 \cdot e^{i2\pi \cdot f_m \cdot (t - \frac{\Delta\phi}{\Delta\omega})} + B_1 \cdot e^{-i2\pi \cdot f_m \cdot (t - \frac{\Delta\phi}{\Delta\omega})}] \qquad \text{(A.3)}
\end{aligned}
$$

The last equation is reasonable if the phase response can be approximated as a linear function. Because the photodetector cannot detect the optical carrier frequency, the reflected sinusoidal signal remains identical to that of the input signal, with a group time delay

$$\tau = \frac{\Delta\phi}{\Delta\omega} \qquad \text{(A.4)}$$

regardless of the altered amplitude factors and the overall phase factor [1, 2]. However, these two terms would not affect the measured light signal delay because the detector measures the light intensity, not the light electric field.

Form (A.3), note that once the reflectivity of one side band is different from the other, or the reflective phase response at these two sideband frequencies is not anti-symmetric with respect to the carrier frequency, then the reflected signal will be distorted.